RESEARCH ARTICLE | MARCH 05 2024

## Alfvénic fluctuations in the expanding solar wind: Formation and radial evolution of spherical polarization •

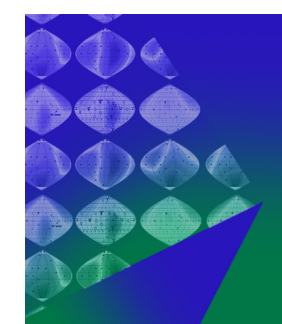
Special Collection: Plasma Physics of the Sun in Honor of Eugene Parker



Phys. Plasmas 31, 032901 (2024) https://doi.org/10.1063/5.0177754







**Physics of Plasmas** 

Features in Plasma Physics Webinars

**Register Today!** 





# Alfvénic fluctuations in the expanding solar wind: Formation and radial evolution of spherical polarization ()

Cite as: Phys. Plasmas **31**, 032901 (2024); doi: 10.1063/5.0177754 Submitted: 24 September 2023 · Accepted: 5 February 2024 · Published Online: 5 March 2024







L. Matteini,<sup>1,a)</sup> (b) A. Tenerani,<sup>2</sup> (b) S. Landi,<sup>3</sup> (b) A. Verdini,<sup>3</sup> (b) M. Velli,<sup>4</sup> (b) P. Hellinger,<sup>1,5</sup> (b) L. Franci,<sup>1,5</sup> (b) T. S. Horbury,<sup>1</sup> (b) E. Papini,<sup>6</sup> (b) and J. E. Stawarz<sup>1,7</sup> (b)

#### **AFFILIATIONS**

- <sup>1</sup>The Blackett Laboratory, Department of Physics, Imperial College London, SW7 2AZ, United Kingdom
- <sup>2</sup>Department of Physics, University of Texas at Austin, Austin, Texas 78712, USA
- <sup>3</sup>Dipartimento di Fisica e Astronomia, Largo Enrico Fermi 2, Firenze 50125, Italy
- $^4$ Department of Earth, Planetary, and Space Sciences, UCLA, Los Angeles, California 90095, USA
- <sup>5</sup>Astronomical Institute, Czech Academy of Sciences, Prague 141 00, Czech Republic
- <sup>6</sup>National Institute for Astrophysics (INAF), Institute for Space Astrophysics and Planetology (IAPS), Rome 00133, Italy
- <sup>7</sup>Department of Mathematics, Physics and Electrical Engineering, Northumbria University, Newcastle upon Tyne NE1 8ST, United Kingdom

Note: This paper is part of the Special Topic: Plasma Physics of the Sun in Honor of Eugene Parker.

a) Author to whom correspondence should be addressed: I.matteini@imperial.ac.uk

#### **ABSTRACT**

We investigate properties of large-scale solar wind Alfvénic fluctuations and their evolution during radial expansion. We assume a strictly radial background magnetic field  $\mathbf{B} \parallel \mathbf{R}$ , and we use two-dimensional hybrid (fluid electrons, kinetic ions) simulations of balanced Alfvénic turbulence in the plane orthogonal to  $\mathbf{B}$ ; the simulated plasma evolves in a system comoving with the solar wind (i.e., in the expanding box approximation). Despite some model limitations, simulations exhibit important properties observed in the solar wind plasma: Magnetic field fluctuations evolve toward a state with low-amplitude variations in the amplitude  $B = |\mathbf{B}|$  and tend to a spherical polarization. This is achieved in the plasma by spontaneously generating field aligned, radial fluctuations that suppress local variations of B, maintaining  $B \sim \text{const.}$  spatially in the plasma. We show that within the constraint of spherical polarization, variations in the radial component of the magnetic field,  $B_R$  lead to a simple relation between  $\delta B_R$  and  $\delta B = |\delta \mathbf{B}|$  as  $\delta B_R \sim \delta B^2/(2B)$ , which correctly describes the observed evolution of the rms of radial fluctuations in the solar wind. During expansion, the background magnetic field amplitude decreases faster than that of fluctuations so that their the relative amplitude increases. In the regime of strong fluctuations,  $\delta B \sim B$ , this causes local magnetic field reversals, consistent with solar wind switchbacks.

© 2024 Author(s). All article content, except where otherwise noted, is licensed under a Creative Commons Attribution (CC BY) license (http://creativecommons.org/licenses/by/4.0/). https://doi.org/10.1063/5.0177754

#### I. INTRODUCTION

Since its first prediction by Parker in 1958<sup>1</sup> and then its detection by spacecraft,<sup>2</sup> the solar wind constitutes a unique laboratory for plasma physics, including fundamental processes such as the nonlinear dynamics of large-amplitude MHD waves and turbulence.<sup>3</sup> Large-scale solar wind fluctuations, especially in the fast wind, are known to be Alfvénic,<sup>4,5</sup> with high correlation degree between changes in the velocity and magnetic field, consistent with a unidirectional flux of anti-sunward Alfvén waves. One of the most remarkable and still

not fully understood properties of the these highly-Alfvénic streams observed at various heliocentric distances from the Sun<sup>5,6</sup> is the fact that low frequency magnetic field fluctuations,  $\delta \mathbf{B}$ , have large amplitudes  $\delta B = |\delta \mathbf{B}|$  which are often of the same order as the underlying magnetic field,  $\delta B \sim |\mathbf{B}_0|$ ; however, the total field magnitude  $B = |\mathbf{B}| = |\mathbf{B}_0 + \delta \mathbf{B}|$  displays a much smaller variance and is observed to remain remarkably constant.

Geometrically, this means that while the direction of the magnetic field vector **B** changes continuously, the tip of the vector stays on a

sphere of approximately constant radius. <sup>7,8</sup> As a consequence, fluctuations cannot be described as simple planar waves. <sup>9</sup> Large amplitude waves propagating in one direction with total field B = const. are an exact solution of the ideal MHD equations (e.g., Refs. 10 and 11), suggesting a sort of local equilibrium in the plasma. How this condition is achieved in the turbulent expanding solar wind and how it is then maintained during expansion in the interplanetary space, is still an open question. Following its geometrical implication, the regime under which the magnetic field fluctuates with little changes in its intensity B is referred to as spherical polarization.

In this work, we use hybrid (fluid electrons, kinetic ions) simulations that include the effect of spherical expansion to investigate the onset of spherical polarization in a solar wind-like plasma with  $\delta B/B \sim 1$  and its evolution with radial distance. We initialize the system with a spectrum of balanced Alfvénic fluctuations (fluctuations with same magnetic and kinetic energy contributions and vanishing cross-helicity), with polarization in the plane orthogonal to the main magnetic radial field  ${\bf B}_0 = B_0 \hat{R}$ . Although this is a reduced and simplified system (2D geometry) and our initial conditions do not capture the whole solar wind complexity, these simulations are remarkably successful in reproducing some of the main properties of spherical polarization and almost constancy of the magnetic field intensity observed in the solar wind plasma.

The paper is organized as follows: first, in Sec. II, we introduce the concept of spherical polarization and summarize its properties as seen in the solar wind. Then, in Sec. III, we recall the main properties of the expanding box model and the expected radial scaling for both background and fluctuating quantities; in Sec. IV, we describe the simulation setup and present results obtained by investigating the evolution of 2D turbulent Alfvénic fluctuations in the expanding solar wind. We then discuss in detail the evolution of fluctuations in the radial (field-aligned) component of the magnetic field and its role in both driving spherical polarization and the generation of magnetic field reversals (switchbacks) that are frequently observed in the near-Sun environment.<sup>12</sup> In Sec. IV D, we show that the evolution observed in simulations, and to a good degree in solar wind observations, is fully characterized by a simple model for  $\delta B_R$  that directly derives from the condition of constant B. We then discuss our results in broader context of solar wind studies in Sec. V and summarize the main achievements of this work as well as future extensions in Sec. VI.

#### II. SPHERICAL POLARIZATION OF ALFVÉN WAVES AND SOLAR WIND OBSERVATIONS

The idea behind the development of spherical polarization is simple and summarized in the cartoon of Fig. 1. Transverse magnetic field fluctuations  $\delta {\bf B}_{\perp}$  with small amplitude  $\delta B_{\perp}$  cause only small changes in the total magnetic field intensity (left); however, if their amplitude grow relatively to the background field  $B_0$  (centre)—as expected for expansion—changes to total  ${\bf B}$  become significant. In a large-amplitude regime, a spatially modulated fluctuating  $\delta B_{\perp}$  would perturb analogously also the total field B. To avoid this, fluctuations can develop a field-aligned component  $\delta {\bf B}_{\parallel}$  as they gradually grow in amplitude, such that the total magnetic field vector is kept on a spherical surface of constant radius B (right), leading to constant intensity B.

Spherical polarization then introduces finite variations  $\delta B_{\parallel} = |\delta {\bf B}_{\parallel}|$ , which can reach  $\delta B_{\parallel} \sim \delta B_{\perp}$ ; however, they do not compress the field; on the contrary, they make the total magnetic field more spatially uniform and the resulting magnetic and plasma

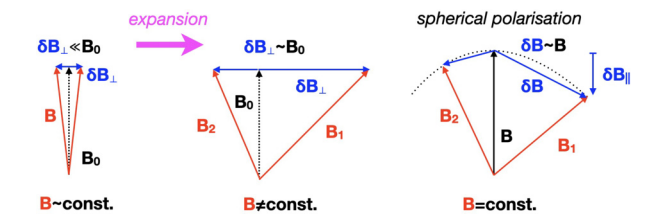


**FIG. 1.** Cartoon showing the evolution of transverse Alfvénic magnetic field fluctuations into spherical polarization with constant total field B. Small amplitude fluctuations (left) can grow relatively to the background field  $B_0$  during solar wind radial expansion, reaching  $\delta B_\perp \sim B_0$  (centre). The subsequent large-amplitude fluctuations are expected to cause big variations in the field intensity, unless variations in the field-aligned component are also developed, maintaining  $\bf B$  on a spherical surface of constant radius  $\bf B$  (right). For large enough  $\delta B_1$  leading to  $\delta B_{||} \sim B_0$ , this process induces the formation of local magnetic field reversals (switchbacks).

pressures are then both constant.<sup>11</sup> Spherical polarization can also be seen as a more general state of arc-polarized Alfvén waves.<sup>13</sup>

Solar wind large amplitude magnetic field fluctuations displaying almost constant magnetic field magnitude are indeed characterized by spherical polarization.<sup>14</sup> An example of this dynamics is shown in Fig. 2, with data from the FIELDS instrument<sup>15</sup> of the Parker solar probe (PSP) during its first perihelion, <sup>16</sup> at approximately 0.15 AU. Observations refer to a subinterval of approximately 6 h with almost constant magnetic field magnitude, when the underlying field  $B_0$  was nearly radial with an average magnitude  $B \sim 80$  nT; however, the same qualitative pattern is observed most of the time in the inner Heliosphere, especially closer to the Sun-see, e.g., Ref. 17 for a more detailed description of the level of spherical polarization observed by PSP. The left panel shows the typical signature of spherical polarization as a scatterplot of the radial and normal components in RTN coordinates; the pattern is the 2D projection of the 3D polarization sphere for the magnetic field vector. To better appreciate the spherical polarization state, the right panel shows the scatterplot of  $B_R$  as a function of the total transverse component  $B_{\perp} = \sqrt{B_T^2 + B_N^2}$ . Data identify a circular shell defined by B = const.; the thickness of the shell provides a measure of the constancy of B.

As a consequence of this dynamics, in the solar wind, during periods of spherical polarization, magnetic field fluctuations can be seen as almost pure rotations of the magnetic field vector; as  $\delta B/B \sim 1$ , they make large angles with respect to the direction of the underlying reference field—here approximately aligned with R as the interplanetary magnetic field is approximately radial near the Sun—and cover a significant fraction of the spherical shell. The portion of the spherical shell covered by the fluctuations varies as a function of heliocentric distance and becomes wider at large distance. Because of this geometrical condition, fluctuations are one-sided in the field-aligned magnetic field component, leading to an asymmetric long tail in its probability density function (PDF) (an example is shown in Sec. IV D of this work and will be discussed later in more detail).

Under the constant B regime just described, if  $\delta B_{\parallel}$  becomes large enough and comparable to  $B_0$ , then they can induce local polarity reversals in the field. Such magnetic structures—called switchbacks—characterized by a local reversal and no, or small,  $^{20,21}$  field compression are very commonly observed in the solar wind, especially in the near-Sun regions. We can indeed appreciate some large

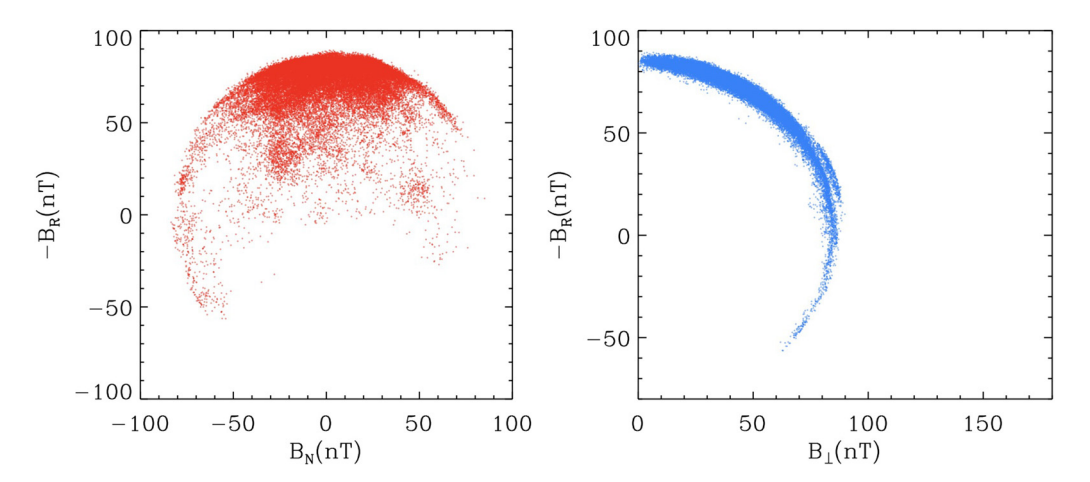


**FIG. 2.** Solar wind magnetic field measurements from the PSP mission during first perihelion at 0.15 AU displaying spherical polarization. Data shown are from a sub-interval with almost constant local magnetic field magnitude. Left: scatterplot of radial  $B_R$  and normal  $B_N$  magnetic field component in RTN. Right: radial  $B_R$  vs orthogonal fluctuations  $B_\perp$ .

excursions of **B** in Fig. 2, leading to local changes in the sign of  $B_R$ . The emergence of spherical polarization, as shown in Fig. 1, then provides a natural way for magnetic field switchbacks to form in the expanding solar wind.  $^{24-27}$ 

While constructing a configuration of large amplitude fluctuations, with spherical polarization—i.e., with at the same time constant  $|\mathbf{B}|$  and  $\nabla \cdot \mathbf{B} = 0$ —can be more easily achieved for structures of lower dimension, it is not trivial in 3D, where discontinuities embedded in the plasma are a frequent, although not necessary, outcome. Interestingly, a numerical method to construct a configuration of spherical polarized fluctuations, which share some similarities with the approach used in this work, has recently been proposed: starting from a low-amplitude configuration, perturbations are grown secularly under the constraint of maintaining constant B. We use a conceptually similar approach, starting from lower amplitude and following expansion while  $\delta B/B$  grows in time; however, the simulation evolves self-consistently and no external constraint is imposed here to the plasma to dynamically preserve B = const..

When considering an initial ensemble of fluctuations with constant magnetic field intensity, even most extreme structures, like switchbacks, remain stable for a long time;<sup>30</sup> this confirms that the constant *B* condition is indeed a long-lasting MHD solution state that can only degrade through wave–wave interactions (e.g., parametric instabilities<sup>31–33</sup>) or kinetic processes that can impact the plasma equilibrium beyond ideal-MHD. Moreover, while spherical polarization can be seen as a local condition, the fact that such a state is maintained during solar wind expansion over a wide range of distances from the Sun, implies that this state not only influences local plasma dynamics but also the overall radial scaling of the fluctuations.

Large-amplitude Alfvénic fluctuations in the solar wind populate the low frequency part of the electromagnetic spectrum, often referred to as the 1/f range (corresponding to scales in the range of tens of minutes to hours). This is considered as the reservoir of energy for a turbulent cascade that extends down to the small kinetic scales of the plasma. While in the 1/f range fluctuations in the transverse components of the magnetic field  $\delta B_{\perp}$  display a WKB-like behaviour  $^{34,35}$  and their power  $\delta B_{\perp}^2$  decays as  $R^{-3}$  consistent with wave-action

conservation, <sup>10</sup> this is typically not observed for the power in the field-aligned component  $\delta B_{\parallel}$ —which can be reasonably identified by  $\delta B_R$  near the Sun, where the interplanetary magnetic field is predominantly radial. Unlike the perpendicular fluctuations, the power of radial magnetic field fluctuations  $\delta B_R^2$  can be found to decay either slower or faster than the adiabatic WKB prediction. <sup>36</sup> This suggests that some different mechanism regulates the evolution of radial fluctuations in the solar wind and the aim of this paper is to characterize it.

### III. THE EXPANDING BOX MODEL AND RADIAL SCALING

## A. The hybrid expanding box (HEB) code and main radial scaling in the model

We use the hybrid-PIC code (kinetic ions, fluid electrons) CAMELIA  $^{37,38}$  with an expanding box model implemented  $^{39,40}$  mimicking the effect of spherical expansion onto the radial motion of a small plasma parcel. The resulting hybrid expanding box (HEB) model  $^{41}$  can then be used to successfully couple large-scale expansion with local microphysics.  $^{42-45}$ 

The expanding box model describes the evolution of a parcel of plasma leaving the Sun with law

$$R = R_0 + Ut, (1)$$

where R is the radial coordinate,  $R_0 = R(t=0)$ ,  $U = R_0/t_{exp}$  is the constant velocity of the expansion, and  $t_{exp}$  is the characteristic expansion time, so that

$$R = R_0(1 + t/t_{exp}). (2)$$

The initial distance from the Sun  $R_0$  doubles after an expansion time  $t_{exp}$ .

While expanding, the size L of the transverse dimensions of the box, here along x and y, grows linearly with distance

$$L_{x,y} \propto R.$$
 (3)

On the contrary, the dimension of the box along the radial,  $L_R$ , remains constant (this is however absent in this work, as limited to 2D).

The code mimics a radial spherical expansion at constant speed U, therefore the number density n scale as

$$n \propto R^{-2}$$
. (4)

We include a strictly radial background magnetic field  $\mathbf{B}_0$ , so that its magnitude  $B_0$  follows:

$$B_0 \propto R^{-2}$$
. (5)

Note that the same scaling applies to the magnitude of the mean field  $\langle \mathbf{B} \rangle$  during the simulation—where the average here and in the rest of the paper means spatial averaging in the box at a given simulation time. In the HEB model, <sup>41,46</sup> a source term appears in the induction equation for  $\mathbf{B}$ , leading to a  $1/R^2$  scaling for the radial component of  $\mathbf{B}_0$  and  $\langle \mathbf{B} \rangle$ , like in the MHD expanding box.<sup>39</sup>

The local Alfvén speed,  $V_A \propto B_0/\sqrt{n}$ , then scales as

$$V_A \propto R^{-1}$$
. (6)

For magnetic flux conservation, in the HEB model, transverse magnetic field components scale as

$$B_{\perp} \propto R^{-1}$$
. (7)

Since we assume a radial background field  $\mathbf{B}_0$ , it then remains radial all the time. Note however that, as discussed below, we expect that transverse fluctuations of the magnetic field initialized on top of  $\mathbf{B}_0$  will evolve according to Eq. (7).

Particle physical scales increase with radial distance R: the initial proton inertial length  $d_{p0}$  is used to normalize length in the simulation, and it scales as  $d_p(R) \propto R$ . Note that this means that, due to Eq. (3), perpendicular scales in the simulation box remain constant in units of the local inertial length,  $L_\perp/d_p=$  const.. This implies that wavevectors of fluctuations orthogonal to  ${\bf B}_0$  maintain the same physical scale during a simulation and so modes initialized at MHD scale at t=0 maintain wavelengths in a constant ratio with ion kinetic scales.

In terms of temporal scales, the unit of time is the inverse of the initial proton cyclotron frequency  $\Omega_{cp0}$ , while the local cyclotron frequency scales as  $\Omega_{cp} \propto R^{-2}$ .

## B. Definition of reference magnetic field and fluctuations

In the simulation, magnetic fields are expressed in units of the underlying background, or main, magnetic field  $\mathbf{B}_0$ , which has magnitude  $B_{0R}=1$  at  $R=R_0$  and decays as  $B_0=B_{0R}/R^2$ . As we initialize the system with in-plane (x,y) magnetic field fluctuations that are statistically axisymmetric and since the background is strictly radial, we have  $\langle B_x \rangle = \langle B_y \rangle = 0$  at all times. Since the average out-of-plane radial component scales as  $\langle B_R \rangle \propto R^{-2}$  because of  $\nabla \cdot \mathbf{B} = 0$ , it therefore means that the mean magnetic field  $\langle \mathbf{B} \rangle$  also scales as  $1/R^2$  and that this can be identified by  $\mathbf{B}_0$ . Fluctuations  $\Delta \mathbf{B}$  can then be defined with respect to  $\mathbf{B}_0$ , such that  $\mathbf{B} = \mathbf{B}_0 + \Delta \mathbf{B}$ , with  $\langle \Delta \mathbf{B} \rangle = 0$ .

On the other hand, the magnitude B decays more slowly than  $B_0$ , because  $|\mathbf{B}| = |\mathbf{B}_0 + \Delta \mathbf{B}|$  and therefore  $B > B_0$  all the time. We can then define a reference  $B_m$  with magnitude  $B_m = \langle B \rangle$  (the average of the magnetic field intensity at each distance R) and directed along R

$$\mathbf{B}_m = B_m \hat{R}. \tag{8}$$

Such a reference field is closer to the one used in observations—where the background field  $\mathbf{B}_0$  is not known *a priori*—to describe spherical polarization and takes into account the fact that also in the simulation, the surface over which we expect spherical polarization has radius B and not  $B_0$ . In terms of  $\mathbf{B}_m$  fluctuations are defined as

$$\mathbf{B} = \mathbf{B}_m + \delta \mathbf{B}. \tag{9}$$

Note that in principle  $\delta \mathbf{B}$  is now different from the previous  $\Delta \mathbf{B}$ . Since the reference field is aligned with  $\hat{R}$ , the difference between  $\Delta \mathbf{B}$  and  $\delta \mathbf{B}$  relies only in the definition of fluctuations along the radial direction  $(\Delta B_{\perp} = \delta B_{\perp})$ . In particular, while  $\langle \Delta B_R \rangle = 0$  by construction,  $\langle \delta B_R \rangle \neq 0$ , reflecting the one-sided nature of field-aligned fluctuations under the constraint of spherical polarization. <sup>19</sup>

In this work, unless differently stated, we will use  $\delta B_R$  as defined by relation (9), as we want to describe magnetic fluctuations as rotations on the sphere; it is then appropriate to consider  $\delta B_R$  as rotation away from  $\mathbf{B}_m$  as defined above, rather than with respect to  $\mathbf{B}_0$ .

#### C. The scaling of magnetic field fluctuations and WKB

Some different scaling with respect to that for the background fields is expected for their fluctuations. In this work, we initialize the system with a set of in-plane Alfvénic-like fluctuations  $\delta \mathbf{B}$  on top of the background out-of-plane  $\mathbf{B}_0 = B_0 \hat{\mathbf{R}}$ . Using the WKB approximation for low frequency MHD Alfvén waves, we can expect that for wave-action conservation, the wave transverse magnetic field fluctuations follow:  $^{10,47}$ 

$$\delta B_{\perp}^2 \propto R^{-3}. \tag{10}$$

For such a scaling in the fluctuations, we expect that for a purely radial background magnetic field, they decay more slowly than the mean field and therefore

$$\delta B_{\perp}/B_0 \propto R^{-1.5}/R^{-2} = \sqrt{R}.$$
 (11)

This scaling is relevant for the near-Sun solar wind above the Alvén radius, in regions where the interplanetary magnetic field can be considered approximatively radial; it predicts the relative level of fluctuations with respect to  $B_0$  to increase with heliocentric distance, approaching  $\delta B_\perp/B_0\sim 1$  during expansion. The scaling of Eq. (11) can indeed be observed near the Sun, inside 0.3 AU, <sup>48</sup> while observations beyond 0.3 AU are consistent with a roughly constant fluctuating level  $\delta B/B$ .

The above scaling is expected for Alfvénic fluctuations that propagate along the background field with parallel k-vectors and finite frequency  $\omega$ . On the other hand, in the 2D reduced geometry used in this work, the main magnetic field  $B_0$  is out of the plane, and we describe only perpendicular k-vectors. Fluctuations then correspond more to an almost zero-frequency set of turbulent fluctuations, orthogonal to  $B_0$ . In the absence of a significant  $k_{\parallel}$ , propagation along the magnetic field is inhibited (although we can still capture some local propagation along projection of bended field lines in the simulation plane), and we do not expect the WKB scaling of relations (10) and (11) to hold. Instead, in our system, for slowly varying, quasi-static Alfvénic structures, we expect the transverse  $\delta B$  to follow the magnetic flux conservation (7) and then

$$\delta B_{\perp} \propto R^{-1}$$
. (12)

This behavior has been indeed checked and confirmed for  $\delta B_{\perp}$  in the simulation.

From initial conditions, in-plane fluctuations dominate the total fluctuating  $\delta B$ , and we expect at all times

$$\delta B \sim \delta B_{\perp} \propto R^{-1}$$
 (13)

this leads then to a different increase in the relative amplitude  $\delta B/B_0$  with respect to the WKB

$$\delta B/B_0 \propto R^{-1}/R^{-2} = R.$$
 (14)

In summary, also in the reduced system, we can expect a constant increase in the relative level of fluctuations, although this is faster than in the propagating WKB case, as from relation (14),  $\delta B/B_0$  increases linearly with R. Note however that this behavior (relative growth of the fluctuations) is still qualitatively similar to what occurs in the real solar wind, while the faster rate at which  $\delta B/B_0$  increases in the simulation allows us to more efficiently capture this effect saving some computational time.

#### D. Fluctuations in the radial component $\delta B_R$

While the radial evolution of the orthogonal magnetic field fluctuations can be reasonably well predicted in terms of scaling discussed in Sec. III C, the evolution of the field aligned fluctuations is less obvious. As we assume a radial background magnetic field, we label the out-of-plane, field aligned fluctuations as  $\delta B_{\parallel} = \delta B_R$  in the following. Note that  $\delta B_R$  fluctuations are absent in the initial condition, however, due to the non-uniform fluctuations  $\delta B$  that are present at t=0, implying some initial modulation of the magnetic field intensity  $|\mathbf{B}|$ , we expect some level of field-aligned fluctuations  $\delta B_R$  to be rapidly generated in the system due to compressive effects.

For magnetic flux conservation, one can expect that fluctuations in  $B_R$  would then decay as the main field  $B_0 \propto R^{-2}$ ; however, this is not what is typically observed in the solar wind plasma, due to the presence of wave couplings. While  $\delta B_R$  would have a  $R^{-2}$  scaling in the absence of any coupling with the velocity field, the fact that  $\delta B_R$  and  $\delta V_R$  can be correlated due to the Alfvénic nature of the structures, introduces some differences. The radial component of the velocity  $V_R$  is expected to remain constant for mass flux conservation, implying the same for its variance  $\delta V_R \sim$  const.. On the other hand, introducing an Alfvénic coupling between  $\delta B_R \propto R^{-2}$  and  $\delta V_R \sqrt{\rho} \propto R^{-1}$ , we can argue that the two fluctuating contributions should adjust on an intermediate radial scaling between -2 and -1,

$$\delta B_R \propto R^{-1.5},$$
 (15)

which, remarkably, is analogous to the solar wind WKB scaling for the transverse  $\delta B_{\perp}$  in Eq. (10). So, in solar wind radial expansion, we can expect variations in all **B** components, at large scale, to decay approximately as WKB. In reality, as already stated, *in situ* observations show that fluctuations in the radial component  $\delta B_R$  follow a somewhat different scaling.

In the simulation scenario here discussed, since  $B_0 \propto R^{-2}$  and  $n \propto R^{-2}$ , we can also expect a behavior close to Eq. (15) to hold for  $\delta B_R$  fluctuations in the case that some effective Alfvénic coupling for the out of plane fluctuations is in place and maintained during

expansion. Alternatively, if  $\delta B_R$  variations are not dynamically coupled to the rest of the fluctuations, we would expect them to decay as fast as  $R^{-2}$ , like the main field  $B_0$ . As we will see in the following, we observe in the simulation, especially at the beginning, a less steep evolution than those above, indicating that in the scenario here investigated,  $\delta B_R$  decays more slowly than expected, or, consistently, that an additional source of field-aligned fluctuations is active during expansion.

#### **IV. HEB RESULTS**

#### A. Simulation setup

We initialize runs with a superposition of in-plane Alfvénic-like fluctuations, with equal energy in magnetic and velocity fields and vanishing cross-helicity. To achieve this, Alfvén modes in Fourier space, each of them with equal velocity  $\delta V_k$  and magnetic field  $\delta B_k$  amplitudes and such that  $\mathbf{k} \cdot \delta \mathbf{V}_k = \mathbf{k} \cdot \delta \mathbf{B}_k = 0$ , are distributed with random phases in physical space. Without expansion, this setup allows for a rapid onset of a turbulent cascade in the simulation, <sup>51,52</sup> with many properties matching solar wind observations.

We have performed multiple runs with different box sizes, spatial resolution, rms amplitude, and plasma beta. All these share analogous evolution and main outcomes; these remain solid also varying the expansion time  $t_{exp}$ . We show and discuss here results from a simulation which is representative of this behavior. The box size is 2128<sup>2</sup> in the plane (x, y), with a spatial resolution of  $\Delta x = \Delta y = 0.5 d_{p0}$ , corresponding to a domain of initial size  $L = 1064d_{p0}$ . Note that this domain mostly covers MHD scales, as we are interested here in the fluid response of the plasma to expansion, and kinetic scales are then not well resolved as we are not interested in sub-ion dynamics. We use 1000 particles-per-cell (ppc) and the initial proton beta is  $\beta_p = 0.1$ ; the electron beta is  $\beta_e = \beta_p$ . The initial spectrum is composed of eight modes in both  $k_x$ ,  $k_y$ , in the range  $[k_{min}, k_{max}]$  with  $k_{min}d_{p0} = 0.006$ and  $k_{max}d_{p0} = 0.047$ ; the amplitude is the same of all modes and equal to  $10^{-2}$ , so that the axisymmetric initial spectrum is  $P(k) \propto k$  and the initial rms of the imposed fluctuations is ~0.23. The background magnetic field  $B_0$  is along the radial direction R, the direction of the solar wind velocity, out of the simulation plane.

We use an expansion time  $t_{exp} = 500\Omega_{cp0}^{-1}$ , where  $\Omega_{cp0}$  is the proton cyclotron frequency in  $R_0$ . For computational reasons, this models a faster expansion than in the real solar wind (a factor 10–100 slower); however, it still ensures a good enough scale separation between slower secular changes occurring on timescales of a fraction of  $t_{exp}$  and proton dynamics which occurs on a few  $\Omega_{cp}^{-1}$ . Moreover, as we focus our investigation on MHD scales, ion-scale effects do not play an important role in the simulation. A faster expansion time is also likely making MHD non-linear interaction slower than in the real solar wind; however, as discussed in the following, we can still see the formation of a turbulent cascade in the simulation, an indication that non-linear interactions are not completely artificially suppressed and can play a role in the dynamics. On the other hand, having a fast enough expansion allows us to explore a wider range of radial distance and to cover a factor 10 in distance in a single simulation. This means that setting  $R_0$  to approximately 0.15 AU (corresponding to first PSP perihelion), we can simulate expansion up to almost 2 AU; this enables comparisons of the results with both near-Sun and past 1 AU observations, ideally with in situ data from PSP, Helios, and Ulysses spacecraft.

#### **B.** Evolution overview

The initial evolution of the simulation is qualitatively similar to the non-expanding case, e.g., Franci et~al.;  $^{51,52}$  initial conditions are quickly relaxed toward a turbulent state, characterized by a broadening of the spectrum of the fluctuations reaching ion scales. During the early stage of this relaxation, various events of magnetic reconnection are typically observed,  $^{53}$  which contribute to the development of a turbulent cascade toward and beyond ion scales.  $^{54,55}$  A Kolmogorov-like power law then develops in the power spectrum of magnetic fluctuations, although the timescale for this process is longer than in the non-expanding case, due to the decay of the amplitude of the fluctuations with distance. We observe a peak in the out-of-plane current (a diagnostic for the strength of turbulent activity) at about  $t \sim 1500\Omega_{cp0}$ , corresponding to  $R \sim 4R_0$ .

Figure 3 shows an overview of the evolution of the fluctuations during the simulation. The left panel shows the in-plane component of the magnetic field fluctuations  $\delta B_{\perp}$  at an intermediate distance  $R=5R_0$ , showing the typical pattern of 2D turbulence, with vortical structures and sheets generated as a result of the relaxation of the initial condition. In the present study, the focus is on larger MHD scales and sub-ion scales are not well resolved; the power spectrum of magnetic fluctuations (shown in the middle panel) is centered on MHD scales, displaying a short inertial range with slope close to -5/3 (the magnetic spectrum shown at the bottom, in red line, is compensated by  $k^{5/3}$ ), followed by a break near  $kd_p \sim 1$ , as expected.<sup>52</sup>

At larger scales, corresponding to the energy injection, the spectrum is characterized by the large-amplitude fluctuations that we address in this work; these are the fluctuations that dominate the rms values that will be discussed in the following. As indicated by the spectrum of the ion velocity (blue line), fluctuations are characterized by an excess of magnetic energy with respect to kinetic. This is a typical feature of 2D MHD turbulence and observed previously in hybrid simulations.<sup>51</sup>

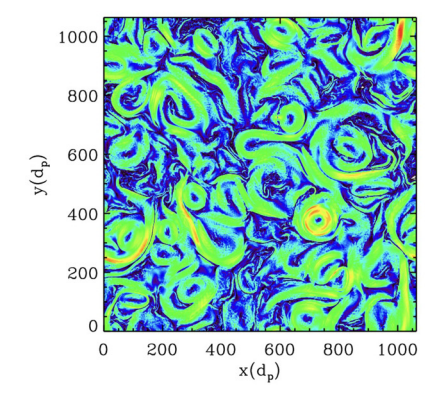
The right panel shows the evolution of the rms of the normalized fluctuations  $\delta B/B$  as a function of radial distance; as expected, the level increases from the initial rms  $\sim$ 0.23 and starts approaching  $\delta B/B \sim 1$  in a few expansion times. In agreement with Eq. (14),

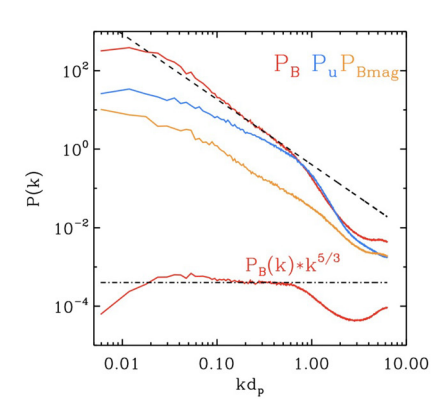
the growth is initially linear (dashed line); however, it starts deviating from the prediction as the level of  $\delta B/B_0$  gradually increases. The dash-dotted line shows the expected evolution for  $\delta B/B$  based on the full magnetic field  $\mathbf{B}=\mathbf{B}_0+\delta\mathbf{B}$ ; as expected, this provides a better description of the evolution when entering a regime where  $\delta B\sim B_0$ . On the other hand, fluctuations in the field magnitude B remain much smaller than those in the components (orange line in the middle panel), confirming a weakly compressible regime. The implications of this behavior will be investigated in detail in Secs. IV C–IV E.

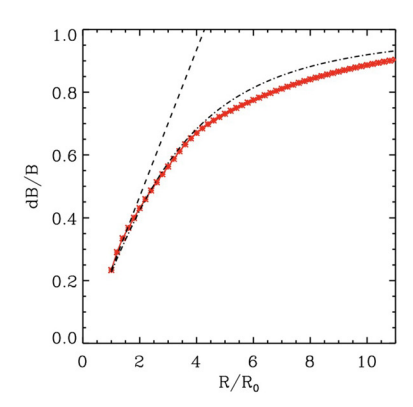
#### C. Radial scaling of the fluctuations

Figure 4 shows a more comprehensive summary of the evolution of the magnetic field and its fluctuations over the whole distance range, shown as average rms values as a function of R. In the top panel, the black and red lines encode the total magnetic field intensity B and the rms of the fluctuations  $\delta B$ . At the beginning, they decay as  $R^{-2}$  and  $R^{-1}$ , respectively, which are the expected scaling according to (5) and (12). This leads to the mentioned increase in  $\delta B/B$ , red line in the bottom panel. The picture changes when  $\delta B$  and B become of the same order. At that point, the magnitude of the total field  $B = |\mathbf{B}|$  $= |\mathbf{B}_0 + \delta \mathbf{B}|$  is no longer scaling as  $R^{-2}$  and starts following a shallower profile, due to the contribution of the fluctuations, which have a slower decay with distance. Eventually, both B and  $\delta B$  adjust on an intermediate scaling that is somewhat between  $R^{-1}$  and  $R^{-1.5}$ ; this later phase corresponds to a slowing down in the growth of  $\delta B/B$ , suggestive of some saturation around unity. Obviously,  $\delta B/B \sim 1$  is the asymptotical limit for when  $\delta B \gg B_0$ , so that  $|\mathbf{B}| \sim |\delta \mathbf{B}|$  and the effect of the mean field  $B_0$  becomes negligible. This stage is however not reached in the simulation—at  $R = 10R_0$ , when  $B_0 = 0.01$  the  $\delta B$  rms is only a factor 2 larger; on the other hand, it is interesting that the change of behavior in  $\delta B/B$  occurs already when  $B \sim \delta B$ .

The blue lines in Fig. 4 refer to the field-aligned radial fluctuations  $\delta B_R$ . These are initially zero, but a finite level of  $\delta B_R$  is quickly generated in the box as a response to the relaxation of the initial conditions. Despite initial modes are Alfvénic and incompressible, their superposition leads to an initial modulation of the total magnetic field B in the box. Shortly after the start of the run, this drives some fast







**FIG. 3.** Overview of the evolution of magnetic fluctuations during expansion. Left: map of the amplitude of the in-plane fluctuations  $\delta B_{\perp}$  at  $R=5R_0$ . Middle: Power spectrum of normalized fluctuations:  $\delta B/B_0$  (red),  $\delta v/V_A$  (blue) and  $\delta |B|/B_0$  (orange), at the same distance  $R=5R_0$  as in the left panel; the magnetic spectrum compensated by  $k^{5/3}$  is shown at the bottom. Right: Evolution of the average level of the fluctuations  $\delta B/B$  as a function of R (red); the dashed line shows the prediction  $\delta B/B_0 \propto R$  [Eq. (14)], while the dash-dotted line refers to the expected evolution of  $\delta B/B$  where R is the total magnetic field intensity (background plus fluctuations).

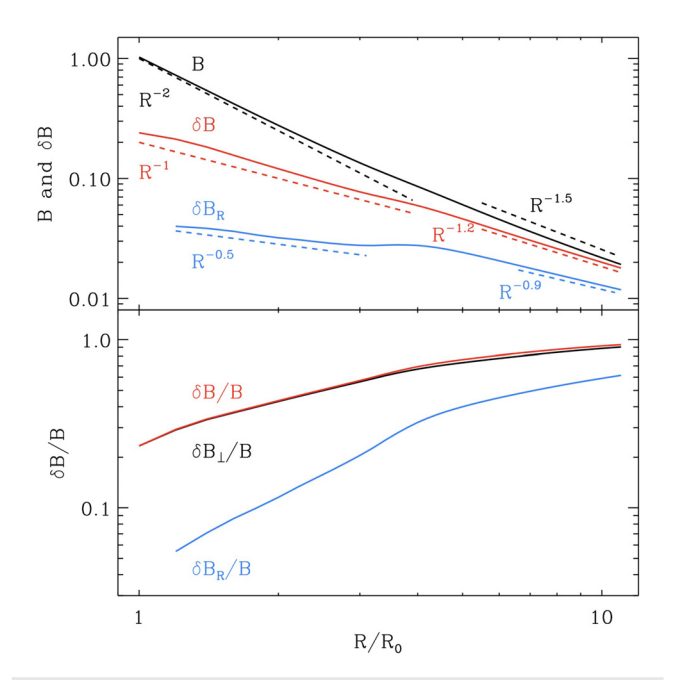


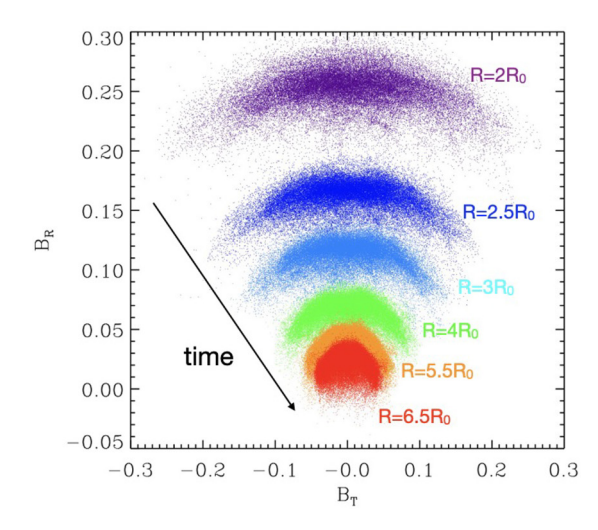
**FIG. 4.** Top panel: radial profile of the total magnitude B (black) and of the rms of the total  $\delta B$  (red) and radial  $\delta B_R$  (blue) fluctuations. Bottom panel: radial profile of the  $\delta B/B$  (red),  $\delta B_{\perp}/B$  (black) and  $\delta B_R/B$  (blue) ratios.

magnetosonic perturbations in the simulation plane that cause the generation of the out-of-plane  $\delta B_R$ . These are identified by a direct correlation between density and field aligned fluctuations in the initial phases—note however that at later times, this compressible coupling in the field-aligned fluctuations is lost in favor of the weakly compressible spherical polarization condition. Once generated, fluctuations in the radial magnetic field component are supported by the turbulent

cascade that is developing but are maintained at a significantly lower amplitude with respect to the dominant transverse components  $\delta B_{\perp}$ . In the first phase of the expansion,  $\delta B_R$  follows a scaling that is significantly less steep than the expected  $R^{-1.5}$  of relation (15), and in the central part of the simulation in particular, there is a strong relative increase in the radial fluctuations ( $\delta B_R$  constant with R), leading to a significant rapid increase in the ratio  $\delta B_R/\delta B$  (bottom panel); such a behavior is analyzed in detail in Secs. IV D and IV E. Finally, similarly to  $\delta B_{\perp}$ , also the ratio  $\delta B_R/B$  approaches a sort of saturation in the last phase. This corresponds to a phase when the radial scaling of  $\delta B_R$  is close to  $R^{-1.5}$ , as it is the case also for  $\delta B$  and B.

#### D. Emergence of spherical polarization

The relative scaling of the fluctuations and the gradual evolution of their polarization can be better appreciated by looking directly at the scatterplot of the magnetic field in a plane that contains  $B_R$  and one of the transverse directions  $B_T$  (either  $B_x$  or  $B_y$ ). This is shown in the left panel of Fig. 5, where different colors encode different radial distances. The amplitude of the fluctuations decays with distance; therefore, the scatterplot pattern shrinks with increasing R. It is interesting to note that an arc-like shape is already visible after 1 expansion time  $(2R_0)$ , suggesting that the plasma starts tending toward a spherical polarization already in the initial stages, when the effects of expansion on  $\delta B/B$  are not too strong yet. As expansion proceeds, the relative importance of variations in  $B_R$  with respect to the initially dominant transverse  $\delta B$  increases; moreover,  $\delta B_R$  variations are correlated with the transverse  $\delta B$  and not symmetric in the resulting change in  $B_{\rm R}$ . Instead, they systematically produce a larger bending of the initial arc-shaped distribution of the data points and the polarization of B corresponds to the projection of a sphere into the plane for larger R. Data points are shown until a distance of  $R = 6.5R_0$ ; as discussed in the following, at larger distances, the shape of the spherical region identified by the points does not change significantly.



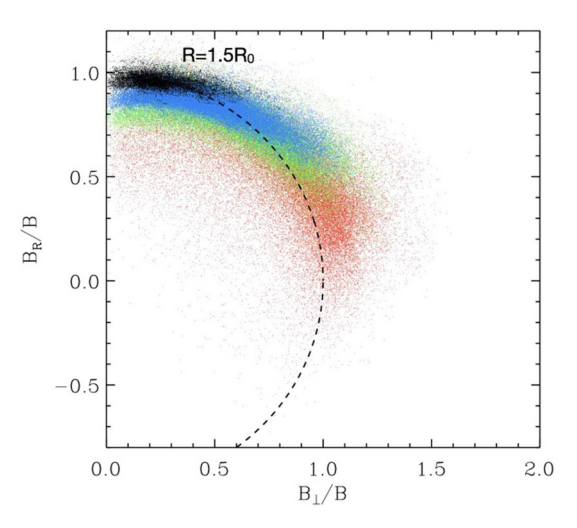


**FIG. 5.** Left panels: Projection of the magnetic fluctuations in the  $(B_T, B_R)$  plane where T is one of the transverse directions, for different radial distances encoded by different colors. A distinct arc-like polarization is visible since the initial stage, evolving toward the 2D projection of a spherical surface at larger distances. Right: projection in the plane  $(B_\perp, B_R)$ , where fluctuations are normalized to the local average magnitude  $\langle B \rangle$  for each R; a subset of distances from the left panel is shown, with the same color code. Black data refer to  $R = 1.5R_0$ .

To better appreciate the gradual emergence of spherical polarization, the right panel of the figure shows an analogous plot, where amplitudes have now been normalized to the local average  $\langle B \rangle$ , so that the background  $B_R$  field is of order 1. In this case, we plot  $B_R$  against the total transverse amplitude  $\delta B_\perp = \sqrt{B_x^2 + B_y^2}$ , to highlight that points approximately lie on a spherical shell of constant radius. This corresponds well to the picture previously discussed using the cartoon of Fig. 1.

At large distances, when reaching the regime  $\delta B \sim B$ , there start to be variations in the radial component  $B_R$  that have same amplitude as the transverse  $B_{\perp}$ . Due to the constraint of spherical polarization, some data points then evolve into negative  $B_R$  values.

Before proceeding further, it is worth considering why spherical polarization emerges so clearly in a system that has low cross-helicity. Indeed, spherical polarization, constant B, is an MHD solution for states at high cross-helicity  $\sigma_{\rm C}$  i.e., dominated by Alfvén waves propagating in only one direction, either parallel or anti-parallel to  ${\bf B}_0$ . A  $|\sigma_c|=1$  regime is characterized by vanishing non-linear interactions in the MHD equations, and therefore, the constant B state is the stable solution discussed in Sec. II. By contrast, a regime with  $\sigma_c\sim 0$  should display strong non-linear interactions (turbulent cascade) and spherical polarization is not a solution.

We initialize the simulation with a set of balanced Alfvénic fluctuations with random phases and vanishing normalized cross-helicity  $\sigma_c = \frac{2\delta \mathbf{v}_\perp \cdot \delta \mathbf{b}_\perp}{\delta \mathbf{v}_\perp^2 + \delta \mathbf{b}_\perp^2}, \text{ where } \delta \mathbf{b} = \delta \mathbf{B}/\sqrt{4\pi\rho}, \text{ with } \rho \text{ the mass density.}^{56,57}$  Initially and at all later times  $\langle \sigma_c \rangle = 0$ , consistent also with the evolution in non-expanding simulations; fluctuations also develop an average negative residual energy—excess of fluctuating magnetic field energy with respect to kinetic energy—also consistent with previous 2D simulations (Fig. 1 in Ref. 51).

The top panel of Fig. 6 shows the PDF of the cosine of the angle  $\theta$ between  $\delta \mathbf{b}_{\perp}$  and  $\delta \mathbf{v}_{\perp}$ ,  $\cos(\theta) = \delta \mathbf{b}_{\perp} \cdot \delta \mathbf{v}_{\perp} / (|\delta \mathbf{b}_{\perp}| |\delta \mathbf{v}_{\perp}|)$ , at the same distance as in Fig. 3 ( $R = 5R_0$ ). We can appreciate that while on average  $\sigma_c$  is zero, transverse fluctuations  $\delta \mathbf{b}_{\perp}$  and  $\delta \mathbf{v}_{\perp}$  are strongly aligned. This if confirmed by the spatial distribution of  $\sigma_c$  in the simulation shown in the middle panel. We can see that since the early phase of the expansion ( $R = 3R_0$ ), fluctuations become organized in regions of high cross-helicity (red and blue patches); this same evolution is seen also without expansion<sup>51</sup> and is consistent with solar wind observations in intervals of balanced turbulence.<sup>58,59</sup> While on average  $\langle \sigma_c \rangle = 0$ , large-scale structures are locally characterized by non-zero positive and negative values of  $\sigma_c$ . These regions of high correlation between  $\delta \mathbf{v}_{\perp}$  and  $\delta \mathbf{b}_{\perp}$  and weaker non-linear terms interact with each other and are bounded by frontiers with  $\sigma_c \sim 0$  where non-linear terms are larger. This offers a more detailed interpretation of the dynamics in the simulation: while the plasma is expanding and  $\delta B/B$ grows, regions of opposite  $\sigma_c$  interact and undergo a turbulent cascade at their boundaries. This leads to the turbulent evolution and the spectrum in Fig. 3; we have indeed verified that, beyond a distance  $R \sim 4R_0$ —when turbulent activity is fully developed—fluctuations at  $kd_p \gtrsim 0.2$  decay faster than geometrical expansion, supporting the presence of an additional turbulent dissipation. By contrast, fluctuations at larger scales continue to decay close to the non-dissipative prediction by Eq. (13) all the time. This is consistent with the fact that according to Fig. 6, large scales are organized in patched of high crosshelicity, and thus do not undergo strong non-linear interactions, do

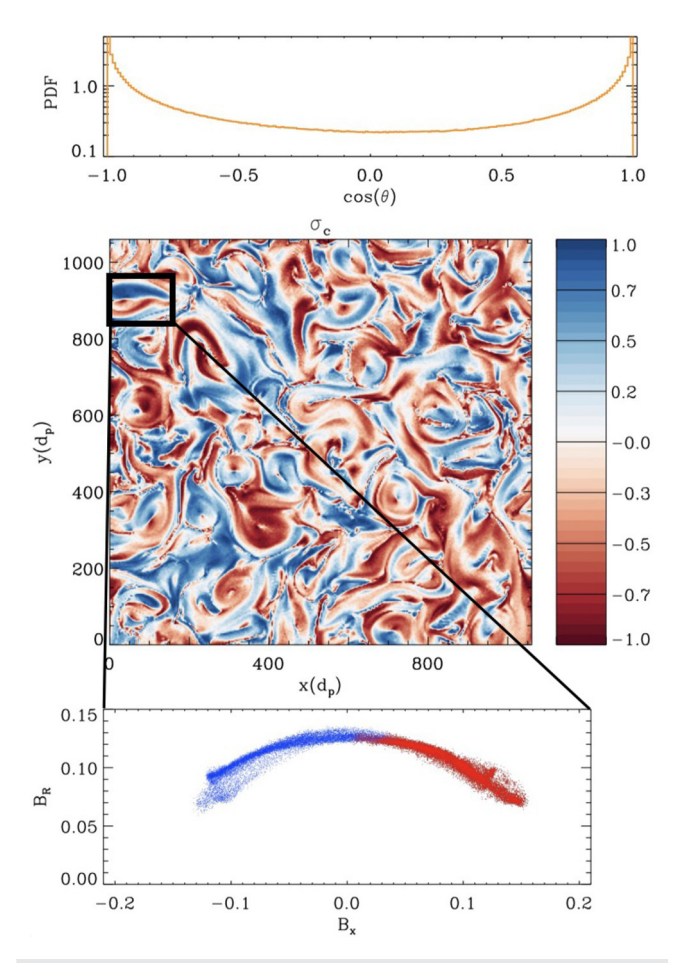


**FIG. 6.** Top panel: PDF of  $\cos{(\theta)}$ , where  $\theta$  is the angle between  $\delta \mathbf{b}_{\perp}$  and  $\delta \mathbf{v}_{\perp}$ , at  $R=5R_0$  (same distance shown in Fig. 3). Middle panel: contour map of  $\sigma_c$  at an earlier stage of the expansion:  $R=3R_0$ . Bottom panel: polarization  $B_{\rm X}-B_{\rm R}$  in the subregion encoded by the black box in the middle panel. In the scatterplot, color blue or red indicate whether points have  $\sigma_c>0$  or  $\sigma_c<0$ , respectively.

not partake into the cascade and survive a long time. These are the fluctuations that then grow to  $dB/B \sim 1$  and dominate in rms values; as they are characterized by weak MHD non-linear terms, they develop spherical polarization as shown in Fig. 5.

An example of one of such magnetic structures is indicated by the black box in the map and shown in the bottom panel. We can appreciate how fluctuations in this large-scale vortex, which displays  $|\sigma_c \sim 1|$  overall, are distributed following an arc shape, indicative of the spherical polarization non-linear solution. Remarkably, this is true for either positive and negative  $\sigma_c$  within the structure (blue and red points in the figure), as there is a change of sign in  $\sigma_c$  within it due to a sign change in  $B_x$  (but not in  $v_x$ ).

#### E. Generation of $\delta B_R$ , evolution and switchbacks

Figure 7 shows the PDF histogram of the radial fluctuations  $\delta B_R$  at different times, encoded with colors from black to red. Values are normalized to the local value of  $B_0$  to highlight the relative change with distance. The distribution is initially narrow and symmetrical around

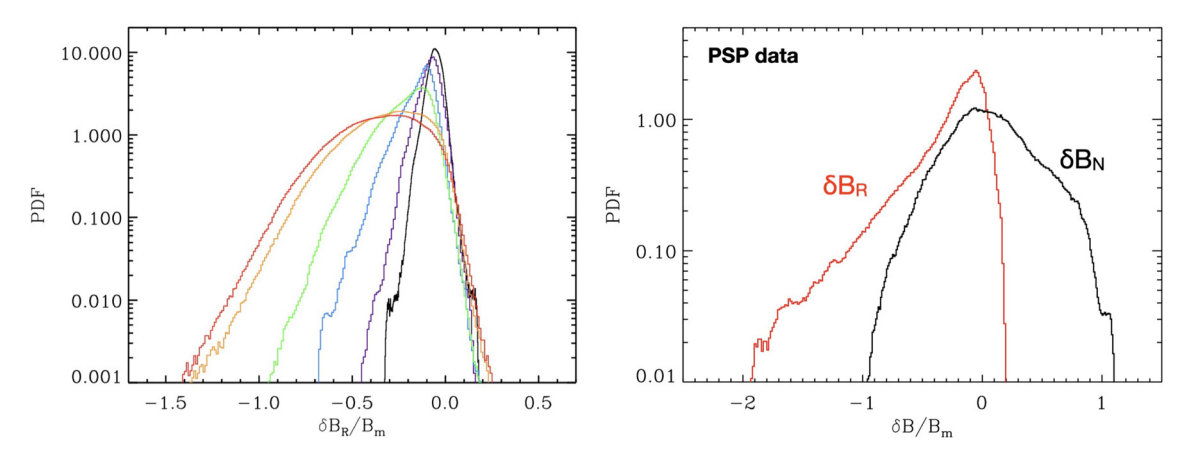


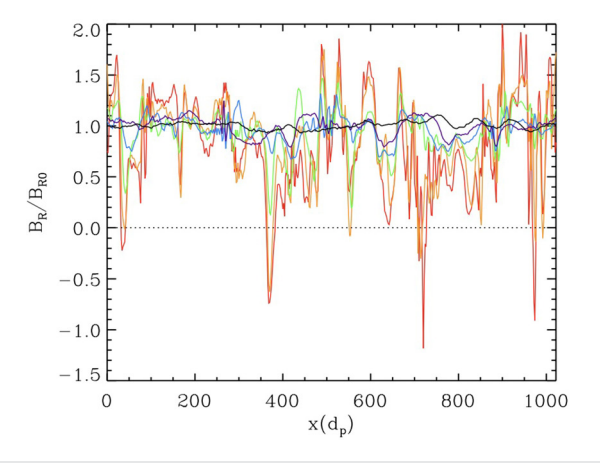
**FIG. 7.** Left: Histogram of the amplitude of the radial fluctuations  $\delta B_R$  as a function of distance and normalized to local  $B_0$ . Different colors encode different R, as in Fig. 5. Right: histogram of the fluctuations in the solar wind radial (red) and normal (black) magnetic field components in RTN coordinate, measured by PSP at first perihelion; fluctuations are normalized to the average magnitude  $B_m = \langle B \rangle$  in the interval and  $\delta B_R$  fluctuations are calculated as described in the text.

zero; this corresponds to the distribution of the small level of radial fluctuations that is generated by relaxation of the initial conditions. As the plasma expands, a wider range of radial fluctuations is generated, in response to the growth of amplitude of the transverse fluctuations  $\delta B_{\perp}$ . The shape of the histogram becomes gradually more asymmetric and a longer tail of negative  $\delta B_R$  arises with distance, as expected for spherical polarization discussed in Sec. II.

For comparison, the right panel of Fig. 7 reports as an example the PDF of solar wind magnetic fluctuations taken over 3 days centered around the first PSP perihelion (discussed in Sec. II), at a distance of 0.15 AU. Note that Fig. 2 displayed a shorter subset of this interval. Fluctuations in the normal and radial components of **B** are shown. Radial  $\delta B_R$  fluctuations are calculated as  $\delta B_R = B_R - B_m$ , where  $B_m$  is the average magnitude  $\langle B \rangle$  in the interval.  $B_m$  corresponds to the average radius of the polarization sphere during the whole interval considered;  $\delta B_R$  so defined are well suited to describe changes in the magnetic field like in Fig. 2—i.e., almost-pure rotations on the

 $B\sim$  const. sphere. To better compare with the left panel, fluctuations have been then normalized to the average magnitude  $B_{mv}$  with a sign change. It is possible to appreciate that with this definition, both  $\delta B_R$  (red) and  $\delta B_N$  (black) PDFs have a peak near zero. While fluctuations in the normal component are approximately symmetric, radial fluctuations are strongly one-sided and have a long asymmetric tail, as required for spherical polarization and consistent with the evolution observed in the simulation. A cutoff at  $|\delta B/B_m|=2$  visible in the PDF of  $\delta B_R$  is also a consequence of spherical polarization.

Note that at larger distances, the tail in the histogram of  $\delta B_R$  in the simulation becomes large enough to reach values of the order of  $-B_0$ . This is consistent with B excursion observed in the solar wind (right panel) and correspond to local reversals of the magnetic field polarity. To explore this feature more in detail, in Fig. 8 (left panel), we show a cut through the simulation box at different times (radial distances); like in Fig. 5, colors from black to red indicate small and large R, respectively. Fluctuations are normalized to the local value of the



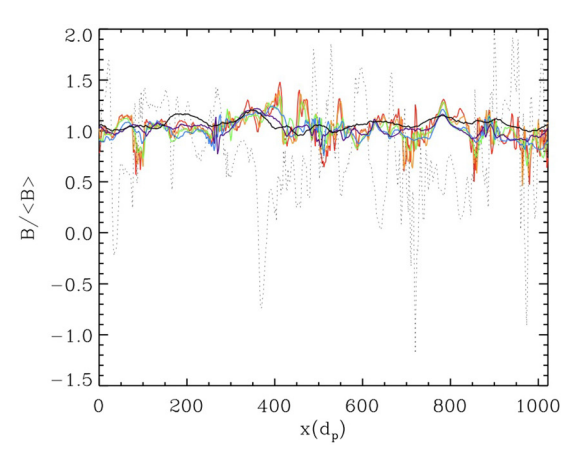


**FIG. 8.** Example of 1D cuts through the simulation box taken at different radial distances; different colors encode different R, as in Fig. 5. Left:  $B_R$  component normalized to the local  $B_{R0}$ . Right: total B, normalized to the average intensity  $\langle B \rangle$  at each R; the thin dashed black profile shown in the right panel encodes the red profile in the left panel, corresponding to the largest distance.

magnetic field  $B_0$ , so that  $B_R \sim 1$  for all profiles. At first (black/purple), we can see that there is little modulation of the radial components of the magnetic field; however, as the amplitude of the turbulent structures is amplified at larger distances (green/blue), we can appreciate again the one-sided nature of the emerging fluctuations: large negative peaks in  $B_R$  are formed (orange/red), some of them bringing the local total  $B_R = B_0 + \delta B_R$  below zero (polarity reversal).

By comparison, the normalized total magnetic field intensity  $B/\langle B\rangle$  (right panel) displays more modest variations, with a much limited growth with radial distance. For reference, note that the two panels have different normalization, as  $|{\bf B}|>B_0$ , due to the presence of fluctuations on top of  ${\bf B_0}$ ; these have been chosen so that resulting normalized quantities are both order 1. Also, note that variations in total B are not necessarily related to a large  $\delta B_R$  modulation; the thin dashed black profile shown in the right panel encodes the red profile in the left panel, corresponding to the largest distance. We can see how the largest variations in B are not always colocated with the largest  $\delta B_R$ —on the contrary places where  $B_R$  reverses have often reasonably smooth B.

To explore more in detail the shape of the structures with largest  $\delta B_R$ , Fig. 9 shows some cuts of typical  $B_R$  reversals through their main axes. The  $B_R$  profile is shown in blue, while the total magnetic field B in black. There are quite small variations in the total intensity B, and they remain of similar amplitude throughout the structure, while on the contrary, the transverse field,  $B_\perp$  undergoes a large modulation,  $\delta B_\perp \sim B$ . As discussed, this is because variations in radial component

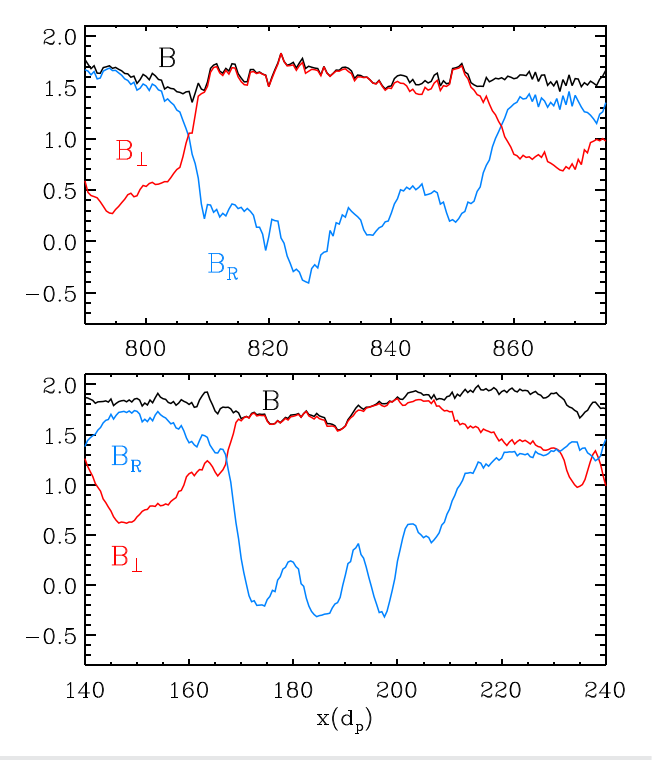


**FIG. 9.** Two examples of particularly large deflections in the magnetic field generated during expansion and associated with a local  $B_R$  reversals. In both panels, local 1D cuts along x in the box show:  $B_R$  (blue),  $B_\perp$  (red) and the total field intensity B (black), normalized to the local  $\hat{B}_0 = B_0/R^2$ . Both examples are for  $R = 6.4R_0$ .

 $B_R$  compensate for the transverse modulation, at least at first order, leading to a less variable total B, such that the magnetic field vector change results overall in a rotation of the field, rather than a compression. Interestingly, the resulting  $B_R$  profile, characterized by a localized region of reversed polarity bounded by two sharp rotations (rotational discontinuities), is consistent with the shape of magnetic switchbacks observed in the solar wind.  $^{16,61}$  Once again, it is a consequence of spherical polarization and the almost constancy of the total magnetic field, as discussed also by Ref. 24.

#### V. MODELING RADIAL FLUCTUATIONS

#### A. A phenomenological model for $\delta B_R$ and constant B

Based on the phenomenological properties described in Sec. IV, it is possible to derive a simple model for the scaling of  $\delta B_R$ . Let us consider first the condition of constancy of the total magnetic field intensity splitting **B** into its radial and transverse components

$$\mathbf{B}^2 = |\mathbf{B}_R + \mathbf{B}_\perp|^2 = B_R^2 + B_\perp^2 = \text{const.}$$
 (16)

Because the constant here is the average value of  $B^2$  and since we have defined  $B_m = \langle B \rangle$ , the relation can be simply rewritten as

$$B_R^2 = B_m^2 - B_\perp^2, (17)$$

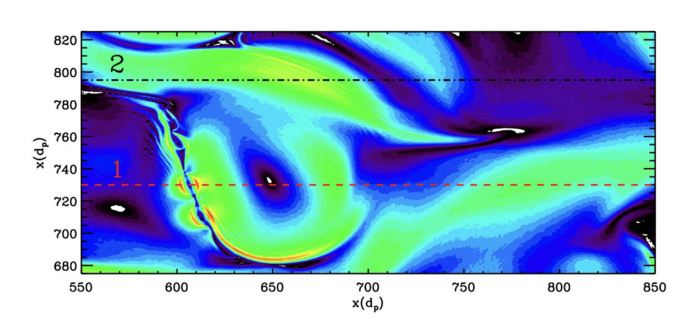
which is simply stating the constraint of spherical polarization for the components. It is clear that in order for this to be satisfied in the domain at each time step,  $B_R$  and  $B_\perp$  need to spatially adjust such that when  $B_\perp$  increases,  $B_R$  decreases, and vice versa. Such variations correspond to pure rotation of the magnetic field vector; the minimum value at the r.h.s. is for  $B_\perp = B_m$ , corresponding to a **B** rotation of 90° from the radial. However, it is still possible for **B** to rotate beyond 90° by changing the sign of  $B_R$ : this is when the rotation becomes a switchback (negative  $B_R$ ).

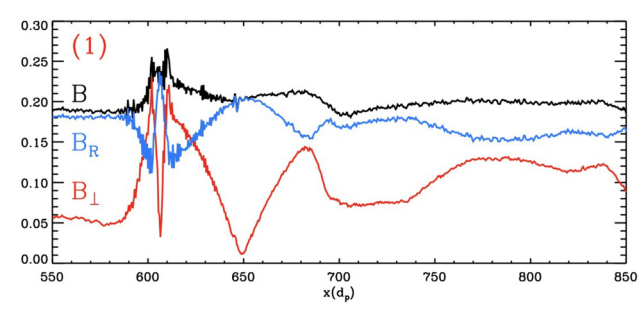
To prove that such a relation holds overall in the simulation since the initial stages, the top panel of Fig. 10 shows a zoom in of a region of the box at t = 700, corresponding to  $R = 2.4R_0$ . The color contour encodes the intensity of  $B_{\perp}$ ; there are large amplitude variations and modulation shown corresponds to structure with  $B_{\perp} \sim B_0$ . The other two panels show some cuts through this region, along the x-axis. In each panel, we show the total field intensity B, the perpendicular component of the field  $B_{\perp}$  (red) and the radial component  $B_R$  (blue); there is a clear anti-correlation between  $B_R$  and  $B_{\perp}$ , such that the resulting total field intensity has a much smaller modulation. Note that this is true for both types of structures present in the plot, vortex-like and sheet-like, such that the examples displayed are representative of the general properties of the magnetic structures in the domain, regardless of their precise shape—spherical polarization is well reproduced everywhere. A possible exception is constituted by sites of magnetic reconnection, like on one of the edges of the vortex shown in the middle panel; we can see that at this localized reconnecting structure the condition  $B \sim \text{const.}$  is less well satisfied—as expected—although there is still a good anti-correlation between  $B_R$  and  $B_{\perp}$ .

We can turn now to considering the constraint on the radial fluctuations  $\delta B_R$ . Let us first split **B** in terms of background field **B**<sub>0</sub> (along the radial direction) and a fluctuating part  $\Delta \mathbf{B}$ , such that  $\Delta \mathbf{B}^2 = \Delta \mathbf{B}_R^2 + \Delta \mathbf{B}_\perp^2$ 

$$\mathbf{B}^{2} = |\mathbf{B}_{0} + \Delta \mathbf{B}|^{2} = B_{0}^{2} + 2\Delta B_{R}B_{0} + \Delta B^{2} = \text{const.}$$
 (18)

This is a quadratic relation for  $\Delta B_R$  and, once again the constant is  $B_m^2$ .





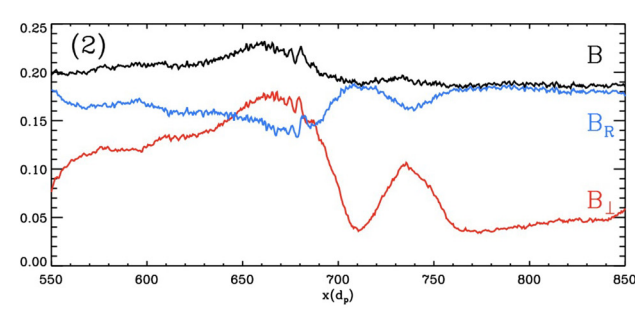


**FIG. 10.** Top panel:  $B\perp$  contour for a subregion of the simulation bow. The dashed and dot-dashed horizontal lines show 1D cuts displayed in the other panels. (Middle) Profiles of B (black),  $B_R$  (blue) and  $B_\perp$  (red) along cut 1. (bottom) Profiles of B,  $B_R$  and  $B_\perp$  along cut 2.

As we want to describe magnetic fluctuations as rotations on the sphere and as done in the rest of the paper, we consider  $\delta B_R$  as rotations away from  $\mathbf{B}_m$ , hence we can write fluctuations as

$$\mathbf{B} = \mathbf{B}_m + \delta \mathbf{B}. \tag{19}$$

Writing the analogous of Eq. (16) using (19), we then have

$$B^2 = B_m^2 + 2\delta B_R B_m + \delta B^2 = \text{const.}$$
 (20)

In this formulation, the constant  $B_m^2$  cancels out and the relation can be simply rewritten as

$$\delta B_R \simeq -\delta B^2 / 2B_m. \tag{21}$$

Remarkably, Eq. (20) directly provides a relation for the amount of fluctuations  $\delta B_R$  that are required in each point in space to balance the main fluctuations  $\delta B$  and ensure then a constant B profile (see also Ref. 25 for a detailed discussion of this formula in the case of propagating Alfvén waves). The constraint of constant magnetic field intensity

 $B^2$  then introduces a local correlation between the amount of fluctuations  $\delta B^2$  and the field-aligned radial component  $\delta B_R$ , with a negative sign.

We can estimate the level of rms radial fluctuations  $\delta B_R^s$  required for spherical polarization as a function of radial distance by then taking the spatial average of Eq. (17) in the simulation box at any distance R

$$\delta B_R^s = \langle \delta B^2 / 2B_m \rangle. \tag{22}$$

Such an estimate of the level  $\delta B_R^s(R)$  can be directly compared to the measured profile of the rms of  $\delta B_R$  in the simulation, to verify how well the phenomenological relation (17) is satisfied.

Figure 11 shows the comparison between  $\delta B_R$  and  $\delta B_R^s$ . The agreement between the predicted about of radial fluctuations  $\delta B_R^s$  (black) and the one measured in the simulation (cyan) is pretty good, and the two curves follow the same radial trend. This suggests that after an initial phase of adjustment when radial fluctuations are generated, they then evolve following relation (17) all the time during expansion. In other words, the amount of fluctuations  $\delta B_R$  supported locally in the plasma at any distance R is constrained by the condition of spherical polarization and is almost exactly the amount needed to maintain structures with B= const. as best as possible for the domain.

#### B. How well is constant B maintained?

To evaluate the level of fluctuations in the magnetic field intensity expected from Eq. (20), we consider the quadratic variations  $\delta(B^2)$   $\equiv B^2 - B_m^2$  as

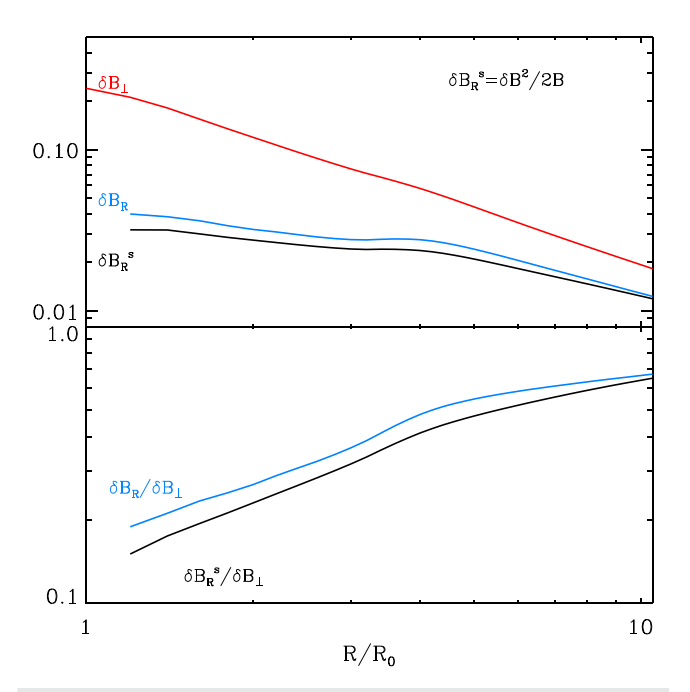


**FIG. 11.** Top panel: Comparison between the measured  $\delta B_R$  (blue) radial profile and the predicted  $\delta B_R^s$  by relation (22) (black); the scaling of  $\delta B_\perp$  (red) is also shown for reference. Lower panel: radial profiles of ratios  $\delta B_R/\delta B_\perp$  and  $\delta B_R^s/\delta B_\perp$  between radial and transverse fluctuations. The ratio is a measure of the spread on the polarization sphere.

$$\delta(B^2) = B^2 - B_m^2 = 2\delta B_R B_m + \delta B^2$$
 (23)

implying that fluctuations in  $B^2$  are directly related to the total level of imposed fluctuations  $\delta B^2$  and the field-aligned perturbation  $\delta B_R$ , through a factor  $2B_m$ . In a small-amplitude regime  $(\delta B \ll B_m)$ , variations in  $B^2$  are linear in the field-aligned perturbations  $\delta B_R$ . In the large-amplitude regime ( $\delta B \sim B_m$ ), we expect  $\delta B^2$ to also contribute. In fact, Fig. 12 shows both terms on the righthand side of Eq. (23),  $\delta B^2$  (black) and  $2\delta B_R B_m$  (red), as average values as a function of R; we can note that, as soon as  $\delta B_R$  fluctuations are generated, the two terms are maintained of the same order all the time. Based on that, one would expect the rms of left-hand side term  $\delta(B^2)$  to be of the same order too; on the contrary, the latter is significantly lower amplitude and drops more quickly with distance. This is because, as discussed, in the r.h.s spatial average  $\langle 2\delta B_R B_m + \delta B^2 \rangle$  the term  $2\delta B_R B_m$  can have a negative sign and locally cancel out with  $\delta B^2$ . This reduces fluctuations in  $B^2$  and keeps the total intensity closer to constant [small  $\delta(B^2)$  on the l.h.s. of (23)], in order to maintain spherical polarization.

How well can then  $B^2=$  const. be maintained? Fig. 12 also shows the radial profile of  $\delta B_R^2$ , which is indeed smaller, as expected since second order in the field-aligned perturbation; we can see that asymptotically, perturbations in the field magnitude  $\delta(B^2)$  adjust to the same level

$$\delta(B^2) \sim \delta B_R^2.$$
 (24)

This seems to be the lowest level of fluctuations in  $B^2$  generated through spherical polarization for a given level of transverse  $\delta B_{\perp}^2$  imposed initially and transported radially by expansion, i.e., without dissipation.

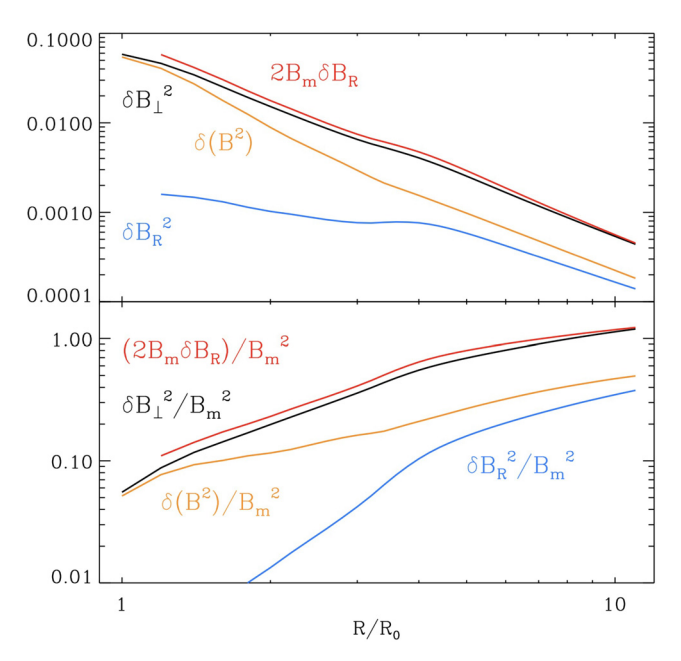


**FIG. 12.** The top panel shows the scaling of the rms of  $\delta B^2$  (black),  $\delta B_R^s$  (red) and of the  $B^2$  fluctuations (orange); the scaling of second order  $\delta B_R^2$  is shown in blue. The lower panel shows the same quantities normalized to the local average magnetic field intensity  $B_m$ .

The lower panel of Fig. 12 shows the square root of quantities in the upper panel normalized to the local average intensity of the field B. A slow increase in  $\delta |B|/B$  with radial distance is also consistent with solar wind observations at larger distance. <sup>17,62</sup>

#### C. Comparison with radial trends observed in situ

Since the simple formula for  $\delta B_R$  based on constant  $B^2$  discussed above can successfully describe the simulation results, we want to check if a similar constraint holds also in the solar wind. Relation (17) can be considered a more general relation for any system where spherical polarization is observed, including then highly Alfvénic solar wind streams. Remarkably, this prediction for  $\delta B_R$  at any R is just based on the scaling for  $\delta B^2$  and B; we can then apply it to observed radial scaling, as those investigated by Tenerani  $et\ al.^{36}$  These authors have found that, in the large-scale 1/f range, while the dominant transverse fluctuations scale closely to the adiabatic WKB prediction in the Alfvénic solar wind, the radial fluctuations can decay either faster or slower than WKB depending on heliocentric distance.

Near the Sun the scaling of the total magnetic field  ${\bf B}={\bf B}_0+\delta {\bf B}$  follows a steeper slope than at larger distances,  $B\propto R^{1.6}$  (see, e.g., Ref. 63) and an almost-WKB scaling  $\delta B_{\perp}^2\propto R^{-3}$  is observed. Using relation (17) to estimate  $\delta B_R$ , it implies:  $\delta B_R=\delta B^2/2B\sim R^{-1.4}$  ( $\delta B_R^2\propto R^{-2.8}$ ), hence less rapidly than  $\delta B_{\perp}^2$  and the WKB prediction. Indeed, this is what is typically observed for the fast solar wind in the inner heliosphere based on Helios observations. On the contrary, in the polar wind observed by Ulysses at larger distances, where the magnitude of the total magnetic field  ${\bf B}$  is observed to decay with a shallower slope, closer to  $B\propto R^{1.4}$  (see, e.g., Ref. 64), a WKB scaling for  $\delta B_{\perp}^2$  implies:  $\delta B_R = \delta B^2/2B\propto R^{-1.6}$ , so faster than  $\delta B_{\perp}$  and the WKB prediction  $R^{-1.5}$ . This is also in agreement with *in situ* observations, where, at larger distances  $\delta B_R^2$  is found to decay faster than  $R^{-3}$  (Ref. 36).

For the same dataset of Ref. 36, authors observed a different evolution for the subset of fluctuations with the largest amplitude (typically switchbacks, with  $\delta B_R \sim \delta B_\perp \sim B$ ). In Helios data, the scaling of  $\delta B_\perp^2$  for switchback is observed to be close to  $R^{-3.4}$ . Coupling this to the scaling of  $B \sim R^{-1.6}$  to get the corresponding prediction for  $\delta B_R$ , we now obtain a faster decay than  $R^{-3}$  also for the radial fluctuations; this is then consistent with the fact that, near the Sun, all components of the field decay faster than WKB when considering only the largest variations/switchbacks. <sup>36</sup>

#### D. Toward the full sphere?

The good agreement of both simulations and solar wind data with the simple relation (17) for the level of radial (field-aligned) fluctuations as a function of distance suggests that this can be used to track the evolution of spherical polarization in the solar wind during expansion. Note that the same would apply to both 2D (arc-like) and 3D (spherical) structures in the plasma. A reasonable question, given the continuous secular increase in  $\delta B_\perp$  with respect to  $B_0$  caused by expansion, is whether the evolution shown in Fig. 5 can continue until fluctuations have a polarization that covers completely the local sphere with constant B. To assess this, an important aspect to consider is the ratio of radial-to-transverse fluctuations  $\delta B_R/\delta B_\perp$ , which represents a measure of the portion of the constant B spherical surface that is populated by the fluctuations as a function of radial distance.

The bottom panel of Fig. 11 shows the evolution of this ratio and compares it to the prediction Eq. (17). After an initial rapid growth, we see that the ratio continues to increase more slowly and tends to saturation. This is consistent with the evolution of  $\delta B/B$  and  $\delta B_R/B$  already discussed in Fig. 4 and can be now revisited according to relation (22): when  $\delta B/B \sim 1$  at large distance, both  $\delta B$  and B, and thus also  $\delta B_R$ —because of the constant B constraint—evolve with approximately similar scaling. The consequence of this behavior is that when  $\delta B/B \sim 1$  all ratios described above tend to a constant value, then slowing down (freezing) changes in the aspect ratio of spherical polarization  $\delta B_R/\delta B_\perp$ .

We argue that this behavior, observed in the simulation, is also consistent with the evolution of spherical polarization observed in the solar wind (see, e.g., Villante<sup>49</sup>). *In situ* observations show that the fluctuating level  $\delta B/B$  is smaller closer to the Sun<sup>48</sup> and so is the portion of the constant B sphere populated by Alfvénic fluctuations. <sup>18</sup> Despite large rotations of **B** with large  $\delta B_R$  leading to polarity changes (switchbacks) are frequent inside 1 AU, 16,65 as shown in Fig. 7, they constitute a tail in the distribution of the rotation angles for measurements close to the Sun; most of the background fluctuations are characterized by smaller rotations,  $^{60}$  corresponding to a smaller average  $\delta B/B$ . At larger distance, the average  $\delta B/B$  grows—as expected from Fig. 4—and fluctuations spread more on the sphere of constant B.18 However, they do not spread over the whole polarization sphere, and in the solar wind fluctuations seem to saturate at a  $\delta B/B$  level with a fixed  $\delta B_R/\delta B_{\perp}$ ratio, which represents the aspect ratio of the observed polarization sphere. This is consistent with our prediction of a slow variation of the  $\delta B_{\perp}/\delta B_R$  ratio when  $\delta B$  and B follow similar radial scaling, and then also  $\delta B \sim \delta B_R$ .

#### VI. DISCUSSION

We review here the main results from this work, as well as its limitations. First, it is remarkable that these simulations naturally evolve toward a regime with more constant total field B and spherical polarization. In particular, it is interesting that this can be achieved in a reduced 2D geometry, where propagation along the mean field is inhibited. This seems to suggest that the state of spherical polarization is a more general regime that can emerge in plasmas with largeamplitude fluctuations, including low cross-helicity states. Its evolution is related to Alfvénicity, but not necessarily linked to propagation and finite parallel k-vectors. We are not suggesting here that our reduced system really captures the complex full-3D expansion dynamics, where additional effects like the rotation of k-vectors due to expansion and the Parker spiral shape of the interplanetary magnetic field can play a role in shaping the evolution. 27,66 Moreover, our initial conditions (orthogonal k-vectors with purely transverse Alfvénic fluctuations, vanishing cross-helicity) may not reproduce appropriately initial conditions of the real solar wind. However, the fact that both systems tend to the same attractor—spherical polarization—despite their differences, suggests that once this is reached, the two descriptions may share several properties. This is promising because it means that we can use this type of simulations to explore further the key processes driving spherical polarization and the regime of almost constant magnetic field intensity in the solar wind.

In fact, despite the fact that the simulation is successful in reaching this regime and the good agreement highlighted in Secs. I-V, a big question remains about the physical causes of such evolution; what really drives constant B and relation (17) in the plasma? This

important question will be subject of some dedicated forthcoming studies. The fact that this regime can be effectively observed in kinetic simulations suggests that its modeling is favored by a kinetic treatment of the plasma (at least in the hybrid approximation including ion kinetics) and in particular by the inclusion of compressible effects associated with the evolution of MHD fluctuations and their possible damping. On the other hand, it has been shown that MHD expanding simulations<sup>24</sup> and modeling including the solar wind acceleration region<sup>26</sup> performed in a fluid compressible regime can recover switchbacks as generated by expansion; this seems to indicate that a fully kinetic description is probably not required and that processes governing the onset of spherical polarization can be-at least partially-of fluid origin. It is also clear that any attempt of describing spherical polarization should include some treatment of field-aligned fluctuations and their coupling with transverse ones, thus suggesting that a model beyond incompressible MHD is needed, at least within the framework analyzed here, as otherwise fluctuations in  $B_R$ —initially absent—would not be generated.

Another aspect to consider concerns the coupling between magnetic and velocity fluctuations. We have seen that spherical polarization in our 2D simulations leads to magnetic field switchbacks. However, the regime here investigated is constituted by an equal amount of counter-propagating Alfvénic fluctuations-vanishing cross-helicity. It is remarkable, and perhaps surprising, that such a  $B \sim \text{const.}$  state can be recovered in a system with balanced Alfvénic fluctuations (zero cross-helicity  $\sigma_c$ ), as spherical polarization is an MHD solution for the state dominated by unidirectional Alfvénic fluctuations, corresponding to  $\sigma_c \pm 1$ . However, we have shown that, within our setup, despite overall  $\langle \sigma_c = 0 \rangle$  in the domain, fluctuations evolve such that large-scale regions of opposite cross-helicity form, each of them characterized by vanishing non-linearities and by local spherical polarization (Fig. 6). This seems to suggest that spherical polarization can be a more general attractor for systems with  $\delta B/B \sim 1$ , not limited to those with high cross-helicity.

On the other hand, an aspect potentially related to cross-helicity and the reduced 2D geometry is that—unlike solar wind switch-backs  $^{22,23,65}$ —in this work,  $B_R$  reversals are not associated with radial velocity enhancements (jets), due to the lack of a strong Alfvénic coupling in the radial magnetic and velocity components. This a known feature of 2D hybrid simulations of Alfvénic turbulence, also without expansion. It is likely that in order to explore further properties of solar wind switchbacks and their kinetics, one should address the high cross-helicity regime and the fully 3D scenario, thus including parallel k-vectors for the fluctuations.

It is also worth stressing that total B is kept constant only to some approximation in our simulations. While in the first part of the runs the emergence of spherical polarization is well characterized by an almost constant magnetic field intensity (see local cuts in Figs. 8–10), the condition of  $B \simeq \text{const.}$  is much less well satisfied in the final stages. In fact, when  $\delta B > B_0$  and  $B \sim \delta B$ , as discussed, relation (17) then implies  $\delta B_R \sim 1/2\delta B$ ; therefore also  $\delta B_R \sim B$  and residual  $\delta B_R^2$  variations are not small anymore compared to B. This may explain why the relative variance of compressive fluctuations  $\delta(B^2)$  shown in the bottom panel of Fig. 12 reaches 50% at the end of the simulation. Note that in the solar wind, despite fluctuations in Alfvénic streams maintain a quite good level of spherical polarization all the time, an increase in  $\delta |\mathbf{B}|/|\mathbf{B}|$  with radial distance is observed.  $^{17,62,68}$ 

We hypothesize that this can be due to the same effect just discussed, although in the simulation the degradation of  $B \sim$  constant occurs earlier due to the faster relative growth of transverse fluctuations with respect to WKB [Eq. (11) vs Eq. (14)].

A parametric study should be performed to identify the regime more favorable for spherical polarization. We have performed preliminary runs with different values of the proton and electron beta, and this will be the subject a forthcoming study. Initial results are reported in Fig. 13 for four runs with different initial proton beta  $\beta_p = 0.02, 0.1, 0.25, 0.5$ , where the last case is the simulation presented in the rest of the paper. The initial electron beta is taken equal to the proton one in each run. The top panel shows the ratio in radialto-perpendicular fluctuations that is measured as a function of the radial distance; the average  $\delta B_R/\delta B_\perp$  at each R provides a measurement of the fraction of the polarization sphere that is populated by fluctuations. Note that as we know that magnetic compressibility (related to the ratio  $\delta B_R/\delta B_{\perp}$ ) in a turbulent MHD cascade is significantly enhanced when transitioning from fluid to ion scales (see, e.g., Ref. 69), in Fig. 13, we have only selected large-scale k-vectors, above the turbulent inertial range and far from ion scales. For example, in the case shown in Fig. 3, fluctuations with k < 0.15. We can see that at large distances, when spherical polarization has developed, the asymptotic level of  $\delta B_R/\delta B_\perp$  is different for each simulation (note that we do not show the first data point, as  $\delta B_R = 0$  in  $R_0$ ). On the other hand, when plotted as a function of  $\beta_p$ , in the lower panel, data points are

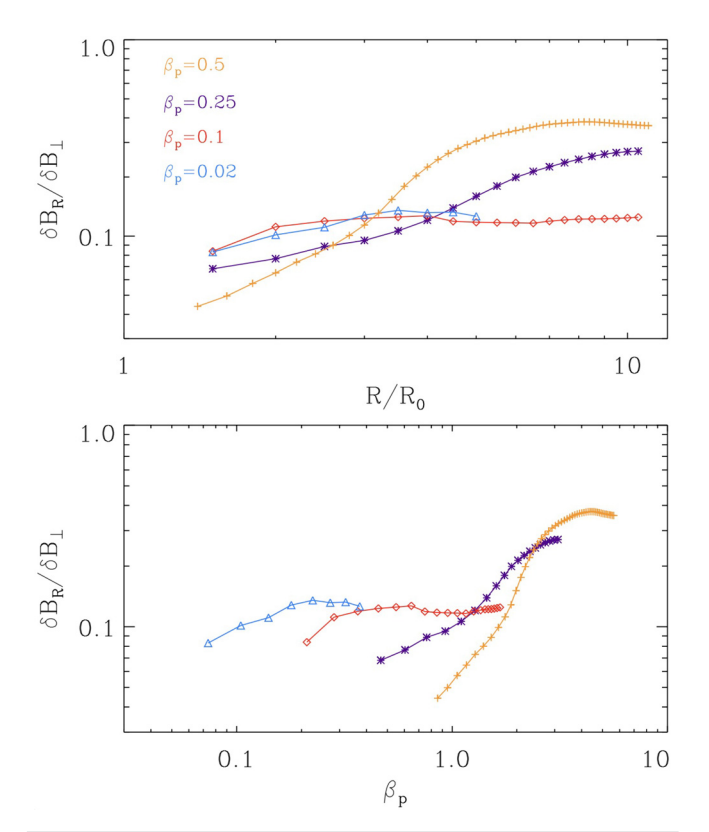


**FIG. 13.** The top panel shows the average ratio of radial to perpendicular fluctuations  $\delta B_R/\delta B_\perp$  as a function of radial distance for four simulations with different initial  $\beta_p$ . The lower panel shows the same quantities as a function of  $\beta_p$ .

better ordered, suggesting that beta plays a role in setting the level of relative radial-to-transverse fluctuations that can be observed, with the largest variation occurring around  $\beta \sim 1$ . Such a dependence on  $\beta$  is potentially consistent with other works<sup>24,25</sup> and will be the subject of future studies.

We conclude this Sec. VI by mentioning that spherical polarization may have an impact also on the statistics of the fluctuations and correlations at large scales. As discussed in Ref. 18, a system with fluctuations homogeneously spread on the full polarization spheremeaning that switchbacks events are as frequent as periods with field along the background direction—would imply some decorrelation in the fluctuations. On the other hand, this does not occur in our simulations, and the system tends to a regime where ratios between the rms of the fluctuations are only slowly changing at larger distance. As a consequence, the portion of sphere populated by magnetic fluctuations gets almost frozen at large distance, preventing the decorrelation process mentioned above. This implies that some finite long-range correlation is maintained among fluctuations at large scales during expansion; some long-range memory is indeed needed to explain the presence of a 1/f range in the solar wind spectrum of Alfvénic fluctuations. Therefore, we suggest that the saturation of spherical polarization seen in simulations, also consistent with solar wind observations, could play a role in the evolution of the large-scale spectrum in the solar wind.

#### VII. CONCLUSION

We have presented results from 2D hybrid expanding box (HEB) simulations of Alfvénic-like fluctuations with an out-of-plane mean magnetic field. Fluctuations start with relatively low amplitude, but their amplitude decreases slower than the background field due to expansion so that they reach large relative amplitudes. We have then studied the evolution with radial distance leading to the emergence of spherical polarization and the formation of polarity reversals (switchbacks). We summarize here below the main finding of this investigation.

First, we have shown that 2D turbulence with Alfvénic-like fluctuations and a mean field  $B_0$  out of the simulation plane naturally evolve toward a state of approximately constant magnetic field intensity and spherical polarization. To our knowledge, this is the first time that is shown and discussed for a kinetic model. Spherical polarization, corresponding to an ideal MHD non-linear solution, is a robust outcome of these runs and is maintained while in-plane fluctuations  $\delta B_{\perp}$  are grown relatively to the mean field by the secular forcing of radial expansion. Remarkably, this state can develop also in a system with zero cross-helicity  $\sigma_{\mathcal{O}}$  as long as local sub-regions of high cross-helicity are formed, consistent with solar wind observations in intervals with overall balanced turbulence, which also show the presence of patches of highly imbalanced states within them.<sup>58</sup>

Second, when the plasma approaches  $\delta B/B \sim 1$ , the amplitude of  $\delta B_R$  fluctuations required to maintain  $B \sim \text{const.}$  increases and leads to regions with  $\delta B_R > B_0$ , so that some polarity reversals are generated locally. These features resemble magnetic field switchbacks seen *in situ* in the solar wind and display some of their main characteristics: large **B** deflections with almost constant magnitude B and  $B_R$  reversals. The mechanism producing these structure by the amplification of pre-existing Alfvénic fluctuations is analogous to that described by MHD models<sup>24–26</sup> and confirms that solar wind switchbacks can be formed by expansion. However, the conditions studied here are different (2D

geometry, no propagation along the main field, vanishing cross-helicity) and then suggest that the generation of magnetic field reversals in a slowing varying magnetic field with increasing  $\delta B/B$  is a more general feature in plasmas and potentially of wider application than the near-Sun solar wind.

Third, the spherical polarization state can be efficiently described by a simple relation (17) for the radial magnetic field fluctuations

$$\delta B_R = -\delta B^2 / 2B. \tag{25}$$

This relation simply states that the condition B = const. holds everywhere in the plasma.  $^{10,11}$  This condition can be used to express the predicted average amount of  $\delta B_R$  fluctuations that can be observed as a function of heliocentric distance in the solar wind just based on the total  $\delta B$  and B. We have verified that the predicted average level  $\delta B_R^s(R)$  is in very good agreement with the rms of  $\delta B_R$  observed in the simulations at all times. Remarkably, this relation reproduces also fairly well the main trend in the radial scaling of the variance of  $\delta B_R$  observed in solar wind streams.  $^{36}$  In particular, it explains the phenomenological result that while the variance of the transverse fluctuations  $\delta B_L$  approximately follow the WKB scaling ( $R^{-1.5}$ ), the radial fluctuations  $\delta B_R$  follow a shallower scaling closer to the Sun (Helios observations) and a steeper one in the polar wind at larger distances (Ulysses).

Finally, we have discussed the asymptotic limit of the scaling and dynamics summarized above. The relative increase in  $\delta B/B$  leads to a stage when  $\delta B \sim B_0$ , meaning that the total magnetic field B has comparable contribution from both the mean field  $B_0$  and the fluctuations. The distance at which this occurs depends obviously on the initial conditions; however, in the simulations, the evolution after this point is such that the total magnetic field intensity  $B = |\mathbf{B}_0 + \delta \mathbf{B}|$  scales with an intermediate law between the mean field  $B_0 \propto R^{-2}$  and  $\delta B \propto R^{-1}$ . This results in B decaying roughly like  $\delta B$  and as a consequence the ratio  $\delta B/B$  tends to saturate near 1 at this stage. The change in the growth of  $\delta B/B$  has an impact also on the ratio  $\delta B_R/\delta B$ , which can be considered a measure of the portion of the polarization sphere populated by the magnetic fluctuations. In fact, the phenomenological relation discussed above,  $\delta B_R = \delta B^2/2B$ , when  $B(R) \sim \delta B(R)$  also implies that  $\delta B_R(R) \sim \delta B(R)$  and then that their ratio becomes frozen. In our opinion, this is an important aspect of the evolution of spherical polarization with distance: in the initial stage of expansion (i.e., in regions closer to the Sun), the continuous growth of  $\delta B/B$  leads to a rapid spread of the magnetic field fluctuations on the polarization sphere; this is well visible in the solar wind by comparing the distribution of **B** on the sphere at different radial distances from the Sun. 18 However, such a trend would lead to a complete and uniform spread of the pattern of the magnetic field vector on the polarization sphere and this is not observed. Instead, Ulysses measurements in the polar wind at larger radial distance suggest that the portion of sphere populated by the fluctuations stops growing at large distances, consistent with the freezing of the aspect ratio  $\delta B_R/\delta B$  found in this work. This aspect will be addressed in a dedicated forthcoming work.

#### **ACKNOWLEDGMENTS**

A.T. acknowledges support from NSF CAREER AWARD No. 2141564. T.H. and L.F. are supported by STFC Grant No. ST/W001071/1. J.E.S. is supported by the Royal Society University

Research Fellowship No. URF/R1/201286. This work was performed using the Cambridge Service for Data Driven Discovery (CSD3), part of which is operated by the University of Cambridge Research Computing on behalf of the STFC DiRAC HPC Facility (www.dirac.ac.uk), under the project dp189 "Plasma kinetics of the expanding solar wind." The DiRAC component of CSD3 was funded by BEIS capital funding via STFC capital Grant Nos. ST/P002307/1 and ST/R002452/1 and STFC operations Grant No. ST/R00689X/1. DiRAC is part of the National e-Infrastructure.

This research was supported by the International Space Science Institute (ISSI) in Bern, through ISSI International Team project #550 "Solar Sources and Evolution of the Alfvénic Slow Wind."

#### **AUTHOR DECLARATIONS**

#### **Conflict of Interest**

The authors have no conflicts to disclose.

#### **Author Contributions**

Lorenzo Matteini: Conceptualization (lead); Formal analysis (lead); Investigation (lead); Methodology (lead); Resources (lead); Writing - original draft (lead); Writing - review & editing (lead). Julia E. Stawarz: Investigation (supporting); Writing – review & editing (supporting). Anna Tenerani: Investigation (supporting); Methodology (supporting); Writing - review & editing (supporting). Simone Landi: Conceptualization (supporting); Investigation (supporting); Methodology (supporting). Andrea Verdini: Conceptualization (supporting); Investigation (supporting); Methodology (supporting); Writing - review & editing (supporting). Marco Velli: Conceptualization (supporting); Investigation (supporting). Petr Hellinger: Investigation (supporting); Methodology (equal); Writing - review & editing (supporting). Luca Franci: Investigation (supporting); Methodology (supporting); Writing - review & editing (supporting). Timothy S. Horbury: Conceptualization (supporting); Investigation (supporting). Emanuele Papini: Investigation (supporting); Writing review & editing (supporting).

#### DATA AVAILABILITY

The data that support the findings of this study are available from the corresponding author upon reasonable request.

#### **REFERENCES**

- <sup>1</sup>E. N. Parker, Astrophys. J. **128**, 664 (1958).
- <sup>2</sup>M. Neugebauer and C. W. Snyder, Science **138**, 1095 (1962).
- <sup>3</sup>R. Bruno and V. Carbone, Living Rev. Sol. Phys. 10, 2 (2013).
- <sup>4</sup>J. W. Belcher and L. Davis, Jr., J. Geophys. Res. 76, 3534, https://doi.org/ 10.1029/JA076i016p03534 (1971).
- <sup>5</sup>E. J. Smith, A. Balogh, M. Neugebauer, and D. McComas, Geophys. Res. Lett. 22, 3381, https://doi.org/10.1029/95GL03268 (1995).
- <sup>6</sup>B. Bavassano and E. J. Smith, J. Geophys. Res. **91**, 1706, https://doi.org/ 10.1029/JA091iA02p01706 (1986).
- <sup>7</sup>A. Barnes, J. Geophys. Res. **86**, 7498, https://doi.org/10.1029/JA086iA09p07498 (1981).
- <sup>8</sup>R. Bruno, V. Carbone, P. Veltri, E. Pietropaolo, and B. Bavassano, Planet. Space Sci. 49, 1201 (2001).
- A. Barnes, J. Geophys. Res. 81, 281, https://doi.org/10.1029/JA081i001p00281 (1976).

- <sup>10</sup>J. V. Hollweg, J. Geophys. Res. **79**, 1539, https://doi.org/10.1029/ JA079i010p01539 (1974).
- <sup>11</sup>A. Barnes and J. V. Hollweg, J. Geophys. Res. **79**, 2302, https://doi.org/10.1029/ JA079i016p02302 (1974).
- <sup>12</sup>N. E. Raouafi, L. Matteini, J. Squire, S. T. Badman, M. Velli, K. G. Klein, C. H. K. Chen, W. H. Matthaeus, A. Szabo, M. Linton, R. C. Allen, J. R. Szalay, R. Bruno, R. B. Decker, M. Akhavan-Tafti, O. V. Agapitov, S. D. Bale, R. Bandyopadhyay, K. Battams, L. Berčič, S. Bourouaine, T. A. Bowen, C. Cattell, B. D. G. Chandran, R. Chhiber, C. M. S. Cohen, R. D'Amicis, J. Giacalone, P. Hess, R. A. Howard, T. S. Horbury, V. K. Jagarlamudi, C. J. Joyce, J. C. Kasper, J. Kinnison, R. Laker, P. Liewer, D. M. Malaspina, I. Mann, D. J. McComas, T. Niembro-Hernandez, T. Nieves-Chinchilla, O. Panasenco, P. Pokorný, A. Pusack, M. Pulupa, J. C. Perez, P. Riley, A. P. Rouillard, C. Shi, G. Stenborg, A. Tenerani, J. L. Verniero, N. Viall, A. Vourlidas, B. E. Wood, L. D. Woodham, and T. Woolley, Space Sci. Rev. 219, 8 (2023).
- <sup>13</sup>B. J. Vasquez and J. V. Hollweg, J. Geophys. Res. **101**, 13527, https://doi.org/ 10.1029/96JA00612 (1996).
- <sup>14</sup>L. Matteini, T. S. Horbury, F. Pantellini, M. Velli, and S. J. Schwartz, Astrophys. J. 802, 11 (2015).
- <sup>15</sup>S. D. Bale, K. Goetz, P. R. Harvey, P. Turin, J. W. Bonnell, T. Dudok de Wit, R. E. Ergun, R. J. MacDowall, M. Pulupa, M. Andre, M. Bolton, J. L. Bougeret, T. A. Bowen, D. Burgess, C. A. Cattell, B. D. G. Chandran, C. C. Chaston, C. H. K. Chen, M. K. Choi, J. E. Connerney, S. Cranmer, M. Diaz-Aguado, W. Donakowski, J. F. Drake, W. M. Farrell, P. Fergeau, J. Fermin, J. Fischer, N. Fox, D. Glaser, M. Goldstein, D. Gordon, E. Hanson, S. E. Harris, L. M. Hayes, J. J. Hinze, J. V. Hollweg, T. S. Horbury, R. A. Howard, V. Hoxie, G. Jannet, M. Karlsson, J. C. Kasper, P. J. Kellogg, M. Kien, J. A. Klimchuk, V. V. Krasnoselskih, S. Krucker, J. J. Lynch, M. Maksimovic, D. M. Malaspina, S. Marker, P. Martin, J. Martinez-Oliveros, J. McCauley, D. J. McComas, T. McDonald, N. Meyer-Vernet, M. Moncuquet, S. J. Monson, F. S. Mozer, S. D. Murphy, J. Odom, R. Oliverson, J. Olson, E. N. Parker, D. Pankow, T. Phan, E. Quataert, T. Quinn, S. W. Ruplin, C. Salem, D. Seitz, D. A. Sheppard, A. Siy, K. Stevens, D. Summers, A. Szabo, M. Timofeeva, A. Vaivads, M. Velli, A. Yehle, D. Werthimer, and J. R. Wygant, Space Sci. Rev. 204, 49 (2016).
- 16 S. D. Bale, S. T. Badman, J. W. Bonnell, T. A. Bowen, D. Burgess, A. W. Case, C. A. Cattell, B. D. G. Chandran, C. C. Chaston, C. H. K. Chen, J. F. Drake, T. D. de Wit, J. P. Eastwood, R. E. Ergun, W. M. Farrell, C. Fong, K. Goetz, M. Goldstein, K. A. Goodrich, P. R. Harvey, T. S. Horbury, G. G. Howes, J. C. Kasper, P. J. Kellogg, J. A. Klimchuk, K. E. Korreck, V. V. Krasnoselskikh, S. Krucker, R. Laker, D. E. Larson, R. J. MacDowall, M. Maksimovic, D. M. Malaspina, J. Martinez-Oliveros, D. J. McComas, N. Meyer-Vernet, M. Moncuquet, F. S. Mozer, T. D. Phan, M. Pulupa, N. E. Raouafi, C. Salem, D. Stansby, M. Stevens, A. Szabo, M. Velli, T. Woolley, and J. R. Wygant, Nature 576, 237 (2019).
- <sup>17</sup>C. Dunn, T. A. Bowen, A. Mallet, S. T. Badman, and S. D. Bale, Astrophys. J. 958, 88 (2023).
- <sup>18</sup>L. Matteini, D. Stansby, T. S. Horbury, and C. H. K. Chen, IL Nuovo Cimento C Geophys. Space Phys. C 42, 16 (2019).
- <sup>19</sup>J. T. Gosling, D. J. McComas, D. A. Roberts, and R. M. Skoug, Astrophys. J. Lett. **695**, L213 (2009).
- <sup>20</sup>W. M. Farrell, R. J. MacDowall, J. R. Gruesbeck, S. D. Bale, and J. C. Kasper, Astrophys. J. 249, 28 (2020).
- <sup>21</sup>A. Larosa, V. Krasnoselskikh, T. Dudok de Wit, O. Agapitov, C. Froment, V. K. Jagarlamudi, M. Velli, S. D. Bale, A. W. Case, K. Goetz, P. Harvey, J. C. Kasper, K. E. Korreck, D. E. Larson, R. J. MacDowall, D. Malaspina, M. Pulupa, C. Revillet, and M. L. Stevens, Astron. Astrophys. 650, A3 (2021).
- <sup>22</sup>L. Matteini, T. S. Horbury, M. Neugebauer, and B. E. Goldstein, Geophys. Res. Lett. 41, 259, https://doi.org/10.1002/2013GL058482 (2014).
- <sup>23</sup>T. S. Horbury, L. Matteini, and D. Stansby, MNRAS **478**, 1980 (2018).
- <sup>24</sup>J. Squire, B. D. G. Chandran, and R. Meyrand, Astrophys. J. Lett. 891, L2 (2020).
- <sup>25</sup>A. Mallet, J. Squire, B. D. G. Chandran, T. Bowen, and S. D. Bale, Astrophys. J. 918, 62 (2021).
- <sup>26</sup>M. Shoda, B. D. G. Chandran, and S. R. Cranmer, Astrophys. J. 915, 52 (2021).
- <sup>27</sup>Z. Johnston, J. Squire, A. Mallet, and R. Meyrand, Phys. Plasmas 29, 072902 (2022).

- <sup>28</sup>F. Valentini, F. Malara, L. Sorriso-Valvo, R. Bruno, and L. Primavera, Astrophys. J. Lett. 881, L5 (2019).
- <sup>29</sup>J. Squire and A. Mallet, J. Plasma Phys. **88**, 175880503 (2022).
- <sup>30</sup>A. Tenerani, M. Velli, L. Matteini, V. Réville, C. Shi, S. D. Bale, J. C. Kasper, J. W. Bonnell, A. W. Case, T. D. de Wit, K. Goetz, P. R. Harvey, K. G. Klein, K. Korreck, D. Larson, R. Livi, R. J. MacDowall, D. M. Malaspina, M. Pulupa, M. Stevens, and P. Whittlesey, Astrophys. J. 246, 32 (2020).
- <sup>31</sup>L. Del Zanna, L. Matteini, S. Landi, A. Verdini, and M. Velli, J. Plasma Phys. 81, 325810102 (2015).
- <sup>32</sup>L. Matteini, S. Landi, L. Del Zanna, M. Velli, and P. Hellinger, Geophys. Res. Lett. 37, L20101, https://doi.org/10.1029/2010GL044806 (2010).
- 33L. Primavera, F. Malara, S. Servidio, G. Nigro, and P. Veltri, Astrophys. J. 880,
- <sup>34</sup>B. Bavassano, M. Dobrowolny, F. Mariani, and N. F. Ness, J. Geophys. Res. 87, 3617, https://doi.org/10.1029/JA087iA05p03617 (1982).
- <sup>35</sup>B. E. Goldstein, E. J. Smith, A. Balogh, T. S. Horbury, M. L. Goldstein, and D. A. Roberts, Geophys. Res. Lett. 22, 3393, https://doi.org/10.1029/95GL03183 (1995).
- 36A. Tenerani, N. Sioulas, L. Matteini, O. Panasenco, C. Shi, and M. Velli, Astrophys. J. Lett. 919, L31 (2021).
- <sup>37</sup>A. Matthews, J. Comput. Phys. **112**, 102 (1994).
- <sup>38</sup>L. Franci, P. Hellinger, M. Guarrasi, C. H. K. Chen, E. Papini, A. Verdini, L. Matteini, and S. Landi, J. Phys. Conf. Ser. 1031, 012002 (2018).
- <sup>39</sup>R. Grappin, M. Velli, and A. Mangeney, *Phys. Rev. Lett.* **70**, 2190 (1993).
- <sup>40</sup>P. C. Liewer, M. Velli, and B. E. Goldstein, J. Geophys. Res. **106**, 29261, https://doi.org/10.1029/2001JA000086 (2001).
- <sup>41</sup>P. Hellinger, P. Trávníček, A. Mangeney, and R. Grappin, Geophys. Res. Lett. 30, 1211, https://doi.org/10.1029/2003GL017855 (2003).
- <sup>42</sup>L. Matteini, S. Landi, P. Hellinger, and M. Velli, J. Geophys. Res. 111, A10101, https://doi.org/10.1029/2006JA011667 (2006).
- <sup>43</sup>L. Matteini, P. Hellinger, S. Landi, P. Trávnícek, and M. Velli, Space Sci. Rev. 172, 373 (2012).
- <sup>44</sup>P. Hellinger, L. Matteini, S. Landi, A. Verdini, L. Franci, and P. M. Trávníček, Astrophys. J. Lett. 811, L32 (2015).
- 45P. Hellinger, L. Matteini, S. Landi, L. Franci, A. Verdini, and E. Papini, Astrophys. J. 883, 178 (2019).
- <sup>46</sup>P. Hellinger and P. Trávníček, J. Geophys. Res. 110, A04210, https://doi.org/ 10.1029/2004JA010687 (2005).
- <sup>47</sup>J. V. Hollweg, J. Geophys. Res. 78, 3643, https://doi.org/10.1029/JA078i019p03643 (1973)
- <sup>48</sup>Z. Huang, N. Sioulas, C. Shi, M. Velli, T. Bowen, N. Davis, B. D. G. Chandran, L. Matteini, N. Kang, X. Shi, J. Huang, S. D. Bale, J. C. Kasper, D. E. Larson, R. Livi, P. L. Whittlesey, A. Rahmati, K. Paulson, M. Stevens, A. W. Case, T. D. de Wit, D. M. Malaspina, J. W. Bonnell, K. Goetz, P. R. Harvey, and R. J. MacDowall, Astrophys. J. Lett. 950, L8 (2023).
- <sup>49</sup>U. Villante, J. Geophys. Res. **85**, 6869, https://doi.org/10.1029/ JA085iA12p06869 (1980).
- 50This is also to highlight analogies with solar wind observations, where the magnetic field is typically measured in RTN coordinates and the radial component is also indicated as  $B_R$ .
- <sup>51</sup>L. Franci, S. Landi, L. Matteini, A. Verdini, and P. Hellinger, Astrophys. J. 812, 21 (2015).
- <sup>52</sup>L. Franci, S. Landi, L. Matteini, A. Verdini, and P. Hellinger, Astrophys. J. 833, 91 (2016).
- <sup>53</sup>L. Franci, S. S. Cerri, F. Califano, S. Landi, E. Papini, A. Verdini, L. Matteini, F. Jenko, and P. Hellinger, Astrophys. J. Lett. 850, L16 (2017).
- <sup>54</sup>P. Hellinger, A. Verdini, S. Landi, L. Franci, and L. Matteini, Astrophys. J. Lett. 857, L19 (2018).
- 55P. Hellinger, V. Montagud-Camps, L. Franci, L. Matteini, E. Papini, A. Verdini, and S. Landi, Astrophys. J. 930, 48 (2022).
- <sup>56</sup>R. Bruno, R. D'Amicis, B. Bavassano, V. Carbone, and L. Sorriso-Valvo, Ann. Geophys. 25, 1913 (2007).
- <sup>57</sup>R. T. Wicks, D. A. Roberts, A. Mallet, A. A. Schekochihin, T. S. Horbury, and C. H. K. Chen, Astrophys. J. **778**, 177 (2013).
- <sup>58</sup>C. H. K. Chen, S. D. Bale, C. S. Salem, and B. A. Maruca, Astrophys. J. 770, 125 (2013).
- <sup>59</sup>S. Servidio, C. Gurgiolo, V. Carbone, and M. L. Goldstein, Astrophys. J. Lett. 789, L44 (2014).

- <sup>60</sup>L. Matteini, D. Stansby, T. S. Horbury, and C. H. K. Chen, Astrophys. J. Lett. 869, L32 (2018).
- <sup>61</sup>T. S. Horbury, T. Woolley, R. Laker, L. Matteini, J. Eastwood, S. D. Bale, M. Velli, B. D. G. Chandran, T. Phan, N. E. Raouafi, K. Goetz, P. R. Harvey, M. Pulupa, K. G. Klein, T. Dudok de Wit, J. C. Kasper, K. E. Korreck, A. W. Case, M. L. Stevens, P. Whittlesey, D. Larson, R. J. MacDowall, D. M. Malaspina, and R. Livi, Astrophys. J. 246, 45 (2020).
- 62T. S. Horbury and A. Balogh, J. Gephys. Res. 106, 15929 (2001).
- 63P. Hellinger, L. Matteini, S. Štverák, P. M. Trávníček, and E. Marsch, J. Geophys. Res. 116, A09105, https://doi.org/10.1029/2011JA016674 (2011).
- <sup>64</sup>B. A. Maruca, R. A. Qudsi, B. L. Alterman, B. M. Walsh, K. E. Korreck, D. Verscharen, R. Bandyopadhyay, R. Chhiber, A. Chasapis, T. N. Parashar, W. H. Matthaeus, and M. L. Goldstein, Astron. Astrophys. 675, A196 (2023).
- <sup>65</sup>J. C. Kasper, S. D. Bale, J. W. Belcher, M. Berthomier, A. W. Case, B. D. G. Chandran, D. W. Curtis, D. Gallagher, S. P. Gary, L. Golub, J. S. Halekas, G. C. Ho, T. S. Horbury, Q. Hu, J. Huang, K. G. Klein, K. E. Korreck, D. E. Larson, R. Livi, B. Maruca, B. Lavraud, P. Louarn, M. Maksimovic, M. Martinovic, D. McGinnis, N. V. Pogorelov, J. D. Richardson, R. M. Skoug, J. T. Steinberg, M. L. Stevens, A. Szabo, M. Velli, P. L. Whittlesey, K. H. Wright, G. P. Zank, R. J. MacDowall, D. J. McComas, R. L. McNutt, M. Pulupa, N. E. Raouafi, and N. A. Schwadron, Nature 576, 228 (2019).
- 66Y. Dong, A. Verdini, and R. Grappin, Astrophys. J. **793**, 118 (2014).
- <sup>67</sup>E. Papini, L. Franci, S. Landi, A. Verdini, L. Matteini, and P. Hellinger, Astrophys. J. 870, 52 (2019).
- <sup>68</sup>B. Bavassano, E. Pietropaolo, and R. Bruno, J. Geophys. Res. **105**, 15959, https://doi.org/10.1029/1999JA000276 (2000).
- <sup>69</sup>L. Matteini, L. Franci, O. Alexandrova, C. Lacombe, S. Landi, P. Hellinger, E. Papini, and A. Verdini, Front. Astron. Space Sci. 7, 83 (2020).